REPORT

SP4 FoU Snøskred

ANNUAL REPORT 2019

DOC.NO. 20170131-17-R
REV.NO. 0 / 2020-05-28

NORWEGIAN GEOTECHNICAL INSTITUTE
NGI.NO

Project

Project title:	SP4 FoU Snøskred
Document title:	Annual Report 2019
Document no.:	20170131-17-R
Date:	2020-05-28
Revision no. /rev. date:	0 /

Client

Client:	Norges vassdrags- og energidirektorat (NVE)
Client contact person:	Aart Verhage and Odd Are Jensen
Contract reference:	Letter from NVE to NGI 2017-11-30

for NGI

Project manager:	Dieter Issler
Prepared by:	Dieter Issler, Peter Gauer, Sylfest Glimsdal, Christian Jaedicke, Frode Sandersen and Kjersti Gleditsch Gisnås
Reviewed by:	Graham Gilbert

NORWEGIAN GEOTECHNICAL INSTITUTE
NGI.NO

Main office
PO Box 3930 Ullevaal St.
NO-0806 Oslo
Norway

Trondheim office
PO Box 5687 Torgarden
NO-7485 Trondheim
Norway

T 22 02 30 00
F 22 23 04 48
NGI@ngi.no

BIC NO. DNBANOKK
IBAN NO26 5096 05 01281
ORGANISATION NO.
958 254 318MVA

ISO 9001/14001
CERTIFIED BY BSI
FS 32989/EMS 612006

p:\2017\01\20170131\leveransedokumenter_og_publikasjoner\2019\rapporter\20170131-17-r_annual_report_2019_final.docx

Summary

NGI has conducted research on avalanches and related processes since 1973. This report gives a short insight in the work done in 2019. While experiments with artificial release of avalanches in the Ryggfonn experimental site were not possible, data was collected on natural avalanche events, both at Ryggfonn and other naturally released avalanches. Work has been done on the statistical approach on avalanche release and runout probability. The feasibility of Voellmy-based numerical models was tested against observed data and simple block models. A three-dimensional CFD model was tested to study the usefulness of detailed physically based wind fields in complex terrain for avalanche mapping and forecasting purposes. The work was presented at several meetings, papers and NGI technical notes which will be made accessible at the project webpage. Taking the results and open questions as well as external input from collaborators and stakeholders into account, the project description for 2020–2022 was elaborated for a successful continuation of the avalanche research.

Contents

Review and reference page

1 Overview and administrative aspects

1.1 Project goals in 2019

The project goals and deliverables for 2019, were only broadly defined in the project proposal. In the Annual Report 2018, a modified task list for 2019 was presented, as shown in Table 1. Bottlenecks in the availability of project members compelled us to adjust the workplan and the list of deliverables (see Sections 2–6 on the work packages).

Table 1 Summary of project goals 2019, based on the project proposal

WP 0	Reporting (Deliverables D0.7–D0.9) Conferences and publications Open workshop about project results 2017–2019 (Deliverable D0.10) Project plan 2020–2022 (Deliverable D0.11)
WP 1	Maintenance of Ryggfonn and Fonnbu (2017–2019) Full-scale experiments at Ryggfonn with artificial release (2017–2019) Deliverable D1.5 – annual report/paper on experiments Contribution to development of dynamical models (2017–2019) Deliverabe D1.6 – annual report/paper on model development
WP 2	StatPack: testing in operational local avalanche forecasting (2018–2019) Deliverable D2.2 – User manual for StatPack and submitted journal paper Impact of mitigation measures on land-use planning (continued from 2018) Deliverable D2.3 – Report/paper on case studies
WP 3	Working setup for SNOWPACK to represent Norwegian wet snow. Prepare recommendations for use of numerical models in slushflow simulations. The Circum-Arctic Slushflow Network: finalize observation guidelines, increase international exchange, support the meeting in Iceland (March 2019).
WP 4	Investigation of interesting snow-avalanche events (2017–2019) Deliverable D4.3 – Annual report/publication on investigated avalanches Detection of snow avalanches by means of infrasound (2017–2019) Deliverable D4.4 – Report/paper on results from infrasound experiment
WP 5	Wind field in mountain topography (continued from 2018) Deliverable D5.1 – Report/paper on WindSim simulations and Winstral model applied to Norwegian mountain areas Quantification of avalanche release probability (2018–2019) Deliverable D5.2 – Report/paper on observed and forecasted release probabilities

1.2 Use of human and financial resources

2019 was a challenging year for FoU Snøskred because several project participants were absent due to maternal leave or illness or left NGI, and others were more occupied in other projects than anticipated. Since in many cases, specific knowledge and competences cannot easily and immediately be supplied by other researchers, we chose to postpone work in the most affected work packages 3 and 5 and use the corresponding resources in WP0 for dissemination, in WP 1 for model development and in WP 2 for further testing and improvement of StatPack.

Table 2 Contributors to the project in 2019, listed alphabetically

Name	**WP**	**Topic**
Hedda Breien	0 4	Webpage content Surveys after avalanche events
Marte F. Busengdal (UiO)	1	Ryggfonn experiment
Regula Frauenfelder	0	Planning 2020–20222
Peter Gauer	0 1 2 3 5	Planning 2020–2022, advising MSc students Leader WP 1, Ryggfonn experiments, data analysis Statistics of avalanche run-out Analysis of slushflow velocity measurements Avalanche release probability
Kjersti Gisnås	0 5	Planning 2020–2022 Climate analysis, WindSim
Sylfest Glimsdal	0 2 5	Advising of MSc students Leader WP 2, implementation of StatPack Tests of WindSim
Håkon Heyerdahl	0	Planning 2020–2022
Graham Gilbert	4	Analysis of infrasound measurements
Dieter Issler	0 1 2 4	Project leader, plan 2020–2022, advisor of MSc student Model development Quality assurance WP 2 Analysis of observed avalanche events
Christian Jaedicke	0 2 3 5	Planning 2020–2022 Quality assurance WP 2 (fuzzy rules) Leader WP 3, CASN Wind field simulations
Krister Kristensen	1	Ryggfonn maintenance and experiment
Henrik Langeland	1	Ryggfonn maintenance and experiment
Erik Lied	1	Maintenance of the Ryggfonn measurement system
Galina Ragulina	0 2	Web page StatPack: fuzzy rules, testing of the release module
Frode Sandersen	0 4	Planning 2020–2022 Leader WP 4
James M. Strout	0	Planning 2020–2022
Kjetil Sverdrup-Thygeson	5	Wind field simulations
Marco Uzielli	2	Statistical and fuzzy methods in StatPack

Table 3 Budgeted and actual allocation of resources per work package in 2019 (in kNOK)

	WP 0	**WP 1**	**WP 2**	**WP 3**	**WP 4**	**WP 5**	**Sum**
Budget 2019	800	1 600	400	300	400	500	4 000
Used 2019	1 490	1 381	379	105	353	292	4 000
Difference	+690	−219	−21	−195	−47	−208	4 000

1.3 Dissemination

(Underlined names refer to project participants)

Presentations at conferences, symposia and meetings

Gauer, P. Avalanche observations related to probabilities. Talk presented at International Symposium on Mitigative Measures against Snow Avalanches and Other Rapid Gravity Mass Flows, Siglufjördur, Iceland, April 3–5, 2019.

Gauer, P. Cross-comparison of Selected Avalanche Observations, Invited talk at International Symposium on Snow Avalanches & Mitigation Strategies, Snow and Avalanche Study Establishment, Chandigarh, India, July 7–9, 2019.

Gauer, P. What can avalanche observations tell us about the performance of numerical avalanche models? Talk presented at Skredkonferansen Voss, Norway, November 1–3, 2019.

Issler, D. Self-consistent models of bed entrainment in gravity mass flows. Talk presented at IUGG General Assembly, Montreal, Canada, July 8–18, 2019.

Issler, D. Excess pore pressure—a unifying concept in gravity mass flow dynamics. Talk presented at IUGG General Assembly, Montreal, Canada, July 8–18, 2019.

Gisnås, K., D. Issler, P. Gauer, C. Jaedicke and S. Glimsdal. Smakebit fra NGIs snøskredforskning. Talk presented at Skredkonferansen Voss, Norway, November 1–3, 2019.

Publications

Gauer, P. (2019). Avalanche observations related to probabilities. *In:* T. Jóhannesson (ed.), Proc. International Symposium on Mitigative Measures against Snow Avalanches and Other Rapid Gravity Mass Flows, Siglufjördur, Iceland, April 3–5, 2019. Icelandic Meteorological Office, Reykjavík, Iceland, pp. 65–71.

Grigorian, S. S. and A. V. Ostroumov (2020). On a continuum model for avalanche flow and its simplified variants. *Geosciences* **10**(1), 35. DOI: 10.3390/geosciences10010035. Edited by D. Issler.

Issler, D. (2020). Comments on "On a continuum model for avalanche flow and its simplified variants" by S. S. Grigorian and A. V. Ostroumov. *Geosciences* **10**(3), 96. DOI: 10.3390/geosciences10030096.

Issler, D., P. Gauer, M. Schaer and S. Keller (2020). Inferences on mixed snow avalanches from field observations. *Geosciences* **10**(1), 2. DOI: 10.3390/geosciences10010002.

Pérez-Guillén, C., K. Tsunematsu, K. Nishimura and D. Issler (2019). Seismic location and tracking of snow avalanches and slush flows on Mt. Fuji, Japan. *Earth Surface Dynamics* **7**, 989–1007. DOI: 10.5194/esurf-7-989-2019.

Ragulina, G., M. Uzielli, S. Glimsdal, M. Rauter and C. Jaedicke (submitted). Estimating Avalanche Triggering Probability using meteorological and local terrain parameters through a fuzzy inference approach.

Reports

Issler, D., Field Survey of the 2017 Rigopiano Avalanche. NGI Technical Note 20170131-08-TN.

Ragulina, G. and M. Uzielli, Estimating Avalanche Triggering Probability using meteorological and local terrain parameters through a fuzzy inference approach. NGI Technical Note 20170131-12-TN.

Sandersen, F. Snøskredulykke i Tamokdalen 2019-01-02 / Snow Avalanche Accident in the Tamok Valley, 2019-01-02. NGI Technical Note 20170131-13-TN rev. 2 [in Norwegian with English summary].

Breien, H., Befaringsrapport Grandefonna, Geiranger [Survey report on the Grandefonna avalanche, Geiranger]. NGI Technical Note 20170131-14-TN [in Norwegian].

Issler, D., Tertialrapport 2019-1. NGI Technical Note 20170131-15-TN [in Norwegian].

Issler, D., Tertialrapport 2019-2. NGI Technical Note 20170131-16-TN [in Norwegian].

Issler, D., P. Gauer, S. Glimsdal, C. Jaedicke, F. Sandersen, K. Gisnås and G. Gilbert, Annual Report 2019. NGI Report 20170131-17-R.

Gilbert, G., Monitoring snow avalanches in Grasdalen using an infrasound array. NGI Technical Note 20170131-18-TN.

2 WP 1 – Full-scale experiments at Ryggfonn and model development

2.1 Maintenance of the full-scale avalanche test site Ryggfonn

Under this task, necessary repairs and updating of the data acquisition system at the Ryggfonn avalanche test site (Stryn municipality, Vestland county, western Norway) were carried out so that the site is ready for the winter season 2019/2020.

Due to budgetary restrictions, for several years this work has been kept at the lowest possible level that keeps the site operational. The need for more thorough maintenance, including replacement of aging parts, is becoming increasingly evident. In 2019, we therefore developed a plan for preventive maintenance that will ensure the site to remain functional and capable of delivering useful measurements for the design of mitigation measures and model development.

This plan will be successively carried out in the upcoming project period, together with a change in the accounting system: The test site Ryggfonn as well as the research station Fonnbu will be administrated as "research resources" ("leiested") independently of this project, i.e., NGI will bear investment and maintenance costs and write them off over suitable periods. Internal and external users will be charged rent for the use of the facilities, making the expenditures more evenly distributed in time and more predictable. The new system will also facilitate participation of external parties from Norway or abroad. Their share of the rent can be in-kind contributions; for example, our research partner BFW in Innsbruck, Austria, has agreed to station one of their new-generation Doppler RADAR systems in Ryggfonn.

2.2 Experimental results from the full-scale test site Ryggfonn

This section constitutes Deliverables D1.3 and D5.2.

2.2.1 Avalanche releases

Several natural avalanches of size 2 to 3 (on the EAWS avalanche size scale) occurred during the winter 2018/2019. The avalanches released during the beginning of January, in February and in a week's period of March. None of the periods were promising for a field campaign. Nonetheless, the situations were unstable enough that in total 9 small to medium-sized avalanches released naturally. Some pressure data could be collected from these events. Those events, however, showed again that it is desirable to have an autonomous RADAR system at the site to obtain velocity data and a system of time lapse cameras to obtain continuous information about the conditions before and after natural releases. Often information about natural releases is missed because field surveys are carried out too late or not at all.

Figure 1–Figure 3 show some examples of the obtained observations. The measurements from the 2019-01-19 event suggest a highly mobile diluted avalanche that just reached the dam.

Figure 1 Avalanche period between 2019-03-19 16:00 and 2019-03-22 03:00. At least four avalanches released in the test-site or in its vicinity during this period.

Figure 2 Natural avalanches in March 2019. Field investigations on 2019-04-12 by Henrik Langeland.

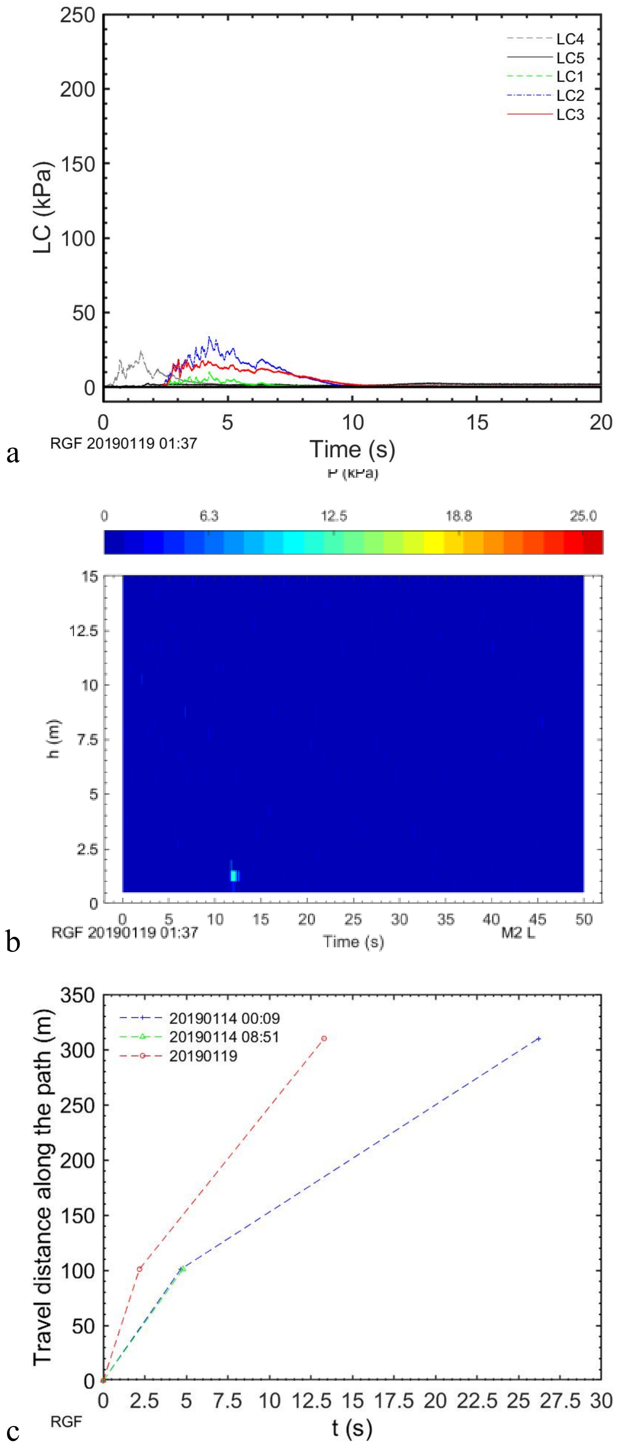

Figure 3 Natural avalanche: a) Pressure measurements at the pylon and concrete wedge (avalanche on 2019-01-19, time off-set not corrected). b) Pressure measurement at mast 2 in front of the dam. c) Timing of the avalanche between pylon, concrete wedge and mast 2 for avalanche events in January 2019.

2.2.2 Data analysis

Avalanche observations related to probabilities

Delineation of avalanche hazard areas or the design of appropriately dimensioned mitigation measures according to the respective regulations while accounting for the possible (economic) consequences is a challenge. Mitigation measures may be very effective for the design event but may have little or no effect on events that exceed the design event. Even if a mitigation measure reduces the hazard in a certain area, an extension of human activity in this area may increase the social risk. Planning and design of avalanche mitigation measures requires information about avalanche intensity (e.g. impact pressure or velocity) and the corresponding occurrence probability.

Probability of natural avalanche release

One of the main challenges regarding hazard assessment is to estimate avalanche probabilities and avalanche sizes for a given path.

Figure 4 shows how precipitation or its intensity may relate to the probability of natural avalanches. It is commonly known that recent loading intensity (either as precipitation or snow drift) is a major driver for natural avalanche activity, however, little work has been done on quantifying this effect. Figure 4 also suggests that especially recent intense loading accounts for high avalanche activity.

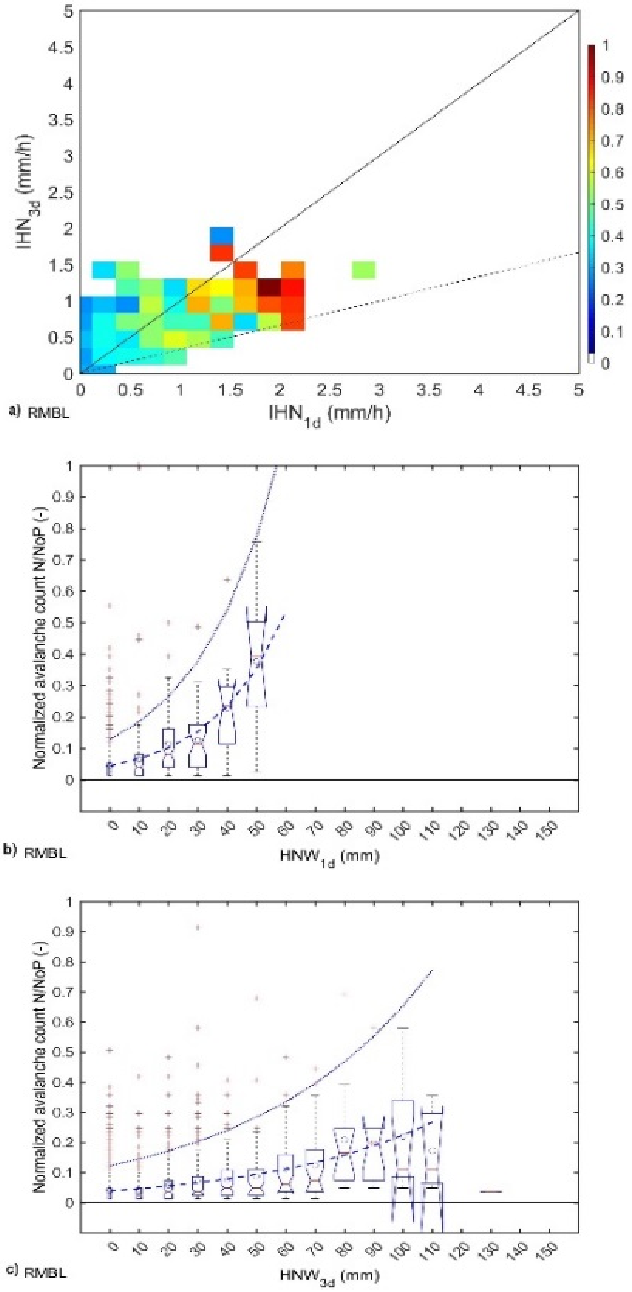

Figure 4 Analysis of weather and avalanche activity observations at the Rocky Mountains Biological Laboratory (RMBL), Gothic, Colorado. a) Normalized conditional probability (log$_{10}$-scaled) of observing an avalanche given the mean precipitation intensity of the last day and last 3 days. The continuous line resamples constant intensity during the last 3 days and the dashed line precipitation only during the last day. b) Normalized number of observed avalanches versus one day new snow water equivalent HNW$_{1d}$ (total number of avalanche paths surveyed NoP = 81). The dashed line shows a fit of the mean value and the dotted line of the 0.95-quantile. c) Normalized number of observed avalanches versus three-day new snow water equivalent HNW$_{3d}$ (number of avalanche paths surveyed NoP = 81).

Fracture depth and avalanche size

In addition to the frequency of an avalanche in a given path, the expected fracture depth and avalanche size/mass are important parameters to consider in hazard assessment. In modern avalanche models, fracture depth and avalanche size are required as initial parameters. Figure 5 shows a collection of observed avalanche deposit sizes versus the total drop height of the avalanche track.

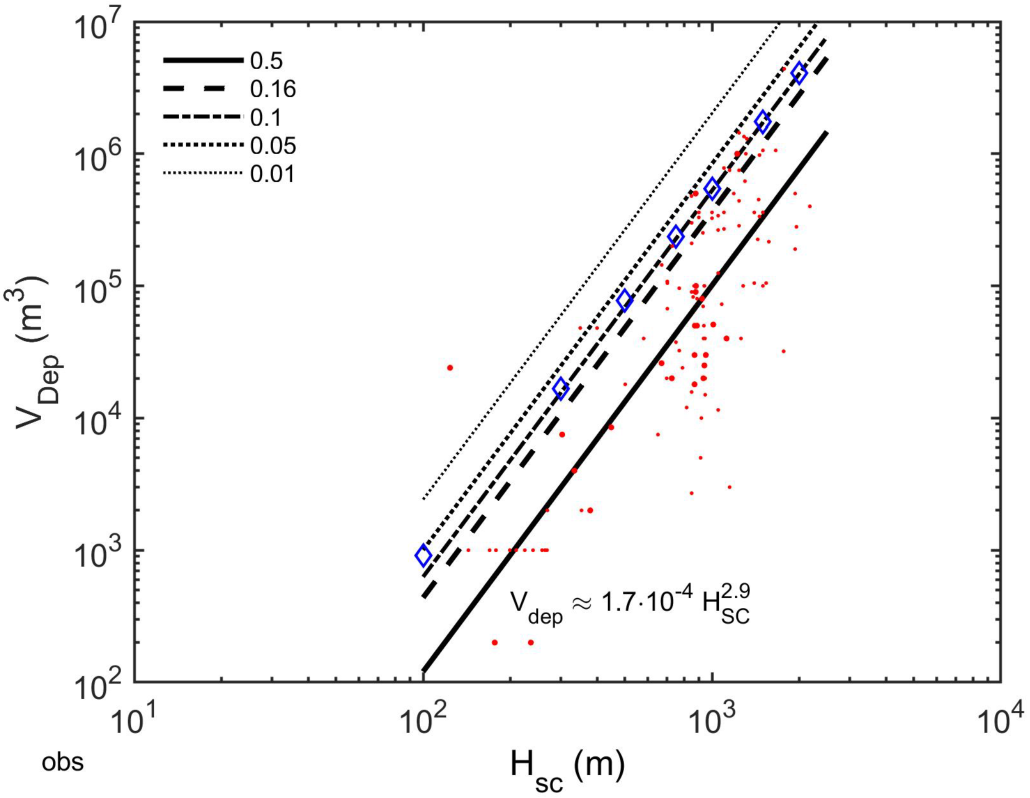

Figure 5 Observed avalanche deposits of "major events" versus total drop height H_{SC} (for references to the data see Gauer et al., 2010). ◊ indicate the volumes used in the RAMMS simulations in the next section. The lines show the estimated exceedance probabilities derived from these observations.

Based on a simple slab model (Lackinger, 1989), Gauer (2018a) used a Monte-Carlo simulation approach to obtain estimates on avalanche release probabilities and probability distributions of the expected fracture depth (snow water equivalent) depending on climatological conditions. In an extension, a similar model was run to include the effects of forest. Figure 6c shows some examples of preliminary results of those Monte-Carlo simulations and comparisons with observations.

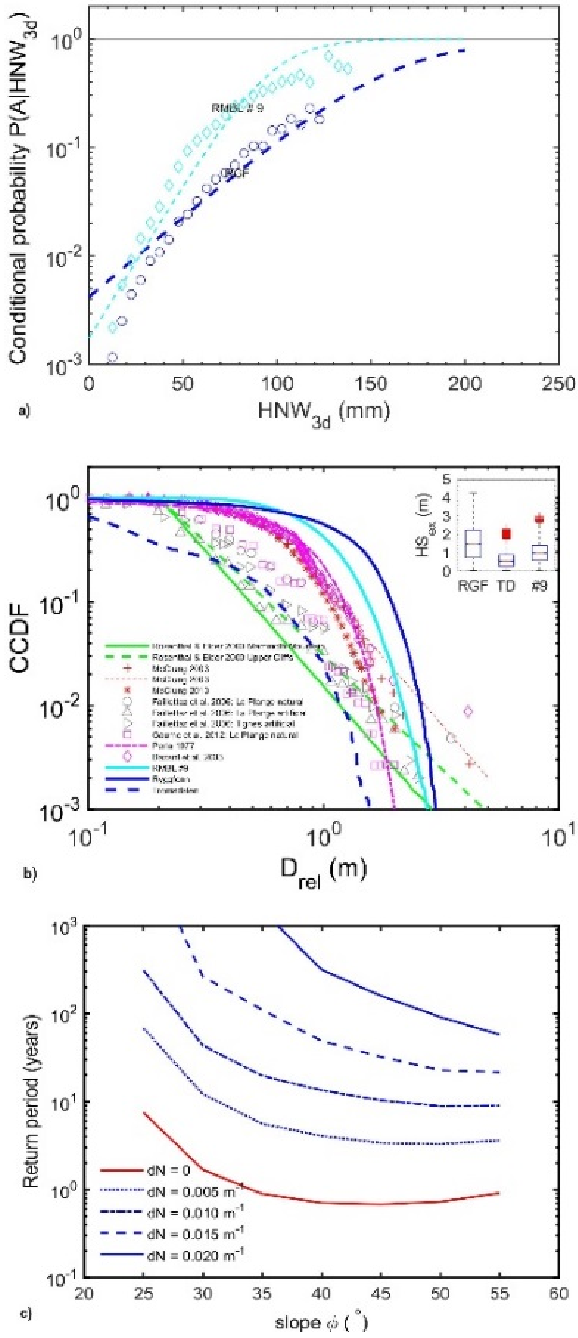

Figure 6 a) Distribution of the conditional probability P(A|HNW$_{3d}$). Comparison of observations (lines) and simulations (dots) for data from Gothic, Colorado (RMBL #9 and Ryggfonn, Norway (RGF). b) Complementary cumulative distribution function of D$_{rel}$. Comparison between simulations for Ryggfonn (RGF, Norway), Tromsdalen (TD, Norway), and Gothic (#9, Colorado) and observations or proposed relations in the literature. The boxplot shows the snow height distributions for the three simulations reflecting different climatic conditions. c) Comparison of the nominal return period versus mean slope angle of the release area with the forest stand factor dN as parameter (dN is given by the breast height diameter in m times the number of trees per m^2).

Scaling behavior of maximum front velocity of major avalanches

Runout observations provide limited constraints for the validation of the empirical parameters used in common present-day numerical avalanche models. This is demonstrated in Figure 7, which shows three simulations with a simple mass-block model governed by the equation of motion

$$\frac{\mathrm{d}U}{\mathrm{d}t} = g(\sin\theta - a_0\cos\theta) - a_2U^2\,, \tag{2.1}$$

where U is the velocity, $\mathrm{d}U/\mathrm{d}t$ the acceleration, g the gravitational acceleration, and ϕ is the slope angle of the track. The model parameters are the Coulomb friction parameter a_0 and the turbulent frictional parameter a_2. Both parameters can be related to the parameters commonly used in the Voellmy model: $\mu = a_0$ and $\xi = g/(a_2\,h_f)$, with h_f the flow depth. We use a simple mass-block model for illustration purposes as it is easy to follow yet is an admissible first-order approximation.

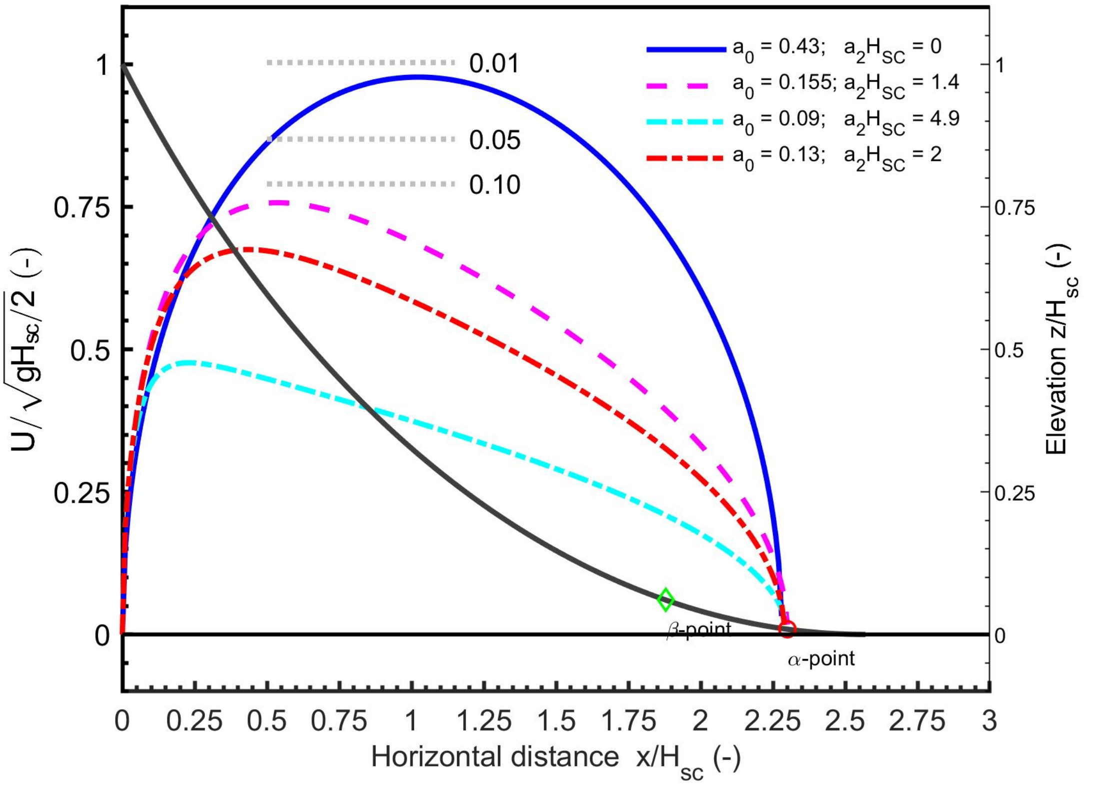

Figure 7 Velocity of a mass block moving with various parameter combinations of {a_0; a_2H_{SC}} along a cycloidal track (black line; steepness in release area is ϕ_0 = 45°) and reaching the α_m-point. The velocity and length are scaled with the total drop height H_{SC}. The gray dotted lines mark the probability of exceedance of the scaled velocity based on observations (cf. Figure 8a).

In the example, all the simulations are forced to reach the expected α-point according to the α-β model (Lied and Bakkehøi, 1980), but depending on the choice of the empirical parameters they show very different velocity distributions along the track. Assuming a flow depth h_f of 2 m and a drop height H_{SC} = 1000 m, the corresponding Voellmy parameters $\{\mu, \xi\}$ are {0.43, ∞}, {0.155, 3500 m s^{-2}}, {0.13, 2450 m s^{-2}}, and {0.09, 1000 m s^{-2}}. This choice of the parameters is inspired by values like $\mu = 0.155$ or $\xi \approx$ 1000 m s^{-2}, or $a_2 H_{SC} = 2$ that can be found in the literature, e.g., (Buser and Frutiger, 1980; Bakkehøi et al., 1983). However, those authors only focused on runout observations.

The differences in the predicted velocities can be crucial for the delimitation of endangered areas or the design of mitigation measures. The latter case is considered in the following example. Simple dimensioning criteria for avalanche catching dams relate the required height of the free board, H_{fb} to the avalanche velocity (see for example Chapter 8.4 in Rudolf-Miklau et al., 2014):

$$H_{fb} = \frac{U^2}{2g\lambda} + h_f\,, \tag{2.2}$$

where λ is an empirical constant with a value typically between 1 and 3, depending on the avalanche type (dry or wet), and h_f is the flow height. In the case of the example in Figure 7, the avalanches stopping at the α_m-point still have a velocity of approximately $0.72\sqrt{gH_{SC}/2}$, $0.4\sqrt{gH_{SC}/2}$, $0.33\sqrt{gH_{SC}/2}$, or $0.21\sqrt{gH_{SC}/2}$, respectively, at the β-point. If one were to plan a catching dam at the β-point, one could directly relate the required freeboard to the drop height H_{SC}:

$$H_{fb} \approx f_v \frac{H_{SC}}{4\lambda} + h_f\,, \tag{2.3}$$

where the factor f_v for our examples is either 0.51, 0.16, 0.11, or 0.04. That is, the design dam height may differ by a factor up to 12, depending on the choice of the model parameters.

Furthermore, the avalanche runtime, which is an important design parameter for some temporal mitigation measures such as automated road closures, may differ considerably. In our example, the runtime,

$$t/\sqrt{H_{SC}/g}, \tag{2.4}$$

varies between approximately 6.3 and 14.7. This factor may determine whether an automated road closure is feasible or not. Hence, not only the prediction of the runout is important but also the correct prediction of the velocity along the path.

Therefore, velocity observations that could constrain model results are desirable. Figure 8a shows the exceedance probability (i.e. the probability of observing a value larger than a given one) for a series of observed values of $U_{\max}/\sqrt{gH_{SC}/2}$ (McClung and Gauer, 2018) and expected α values according to the α-β model (Lied and Bakkehøi, 1980). The assumption of the empirical α-β model is that the data behind it reflect rare avalanches—events with return periods of the order of 100 years. With that in mind, exceedance probability in Figure 8b might be multiplied by a factor of the order of 10^{-2} to obtain annual probabilities. The complementary cumulative distribution function (CCDF) of U_{max} can be approximated reasonably well by a Generalized Extreme Value (GEV) distribution.

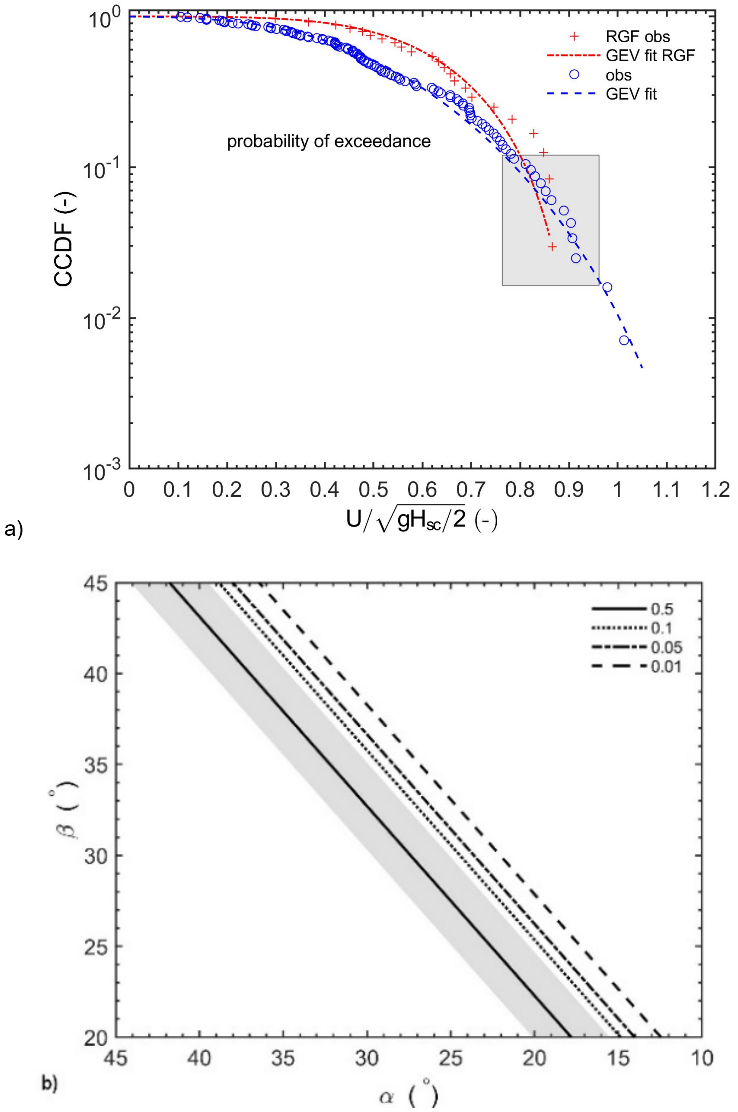

Figure 8 a) Complementary Cumulative Distribution Function (CCDF, survivor function) of observed values of $U_{max}/\sqrt{gH_{SC}/2}$ at Ryggfonn and major avalanches at various locations. The gray rectangle indicates a region that covers typical rare events (cf. Figure 9); and b) estimated exceedance probability of α versus β according to the α-β model (Lied and Bakkehøi, 1980) for major avalanche events.

Figure 9a shows the calculated (dimensionless) velocity of a mass block moving with a constant retarding acceleration along a cycloidal track. The retarding acceleration is chosen in such a way that the mass block stops at, respectively, the β-point (which is close to the $\alpha_{\mathrm{m}}+1\sigma$ -point), the α_{m}-point, or the $\alpha_{\mathrm{m}}-1\sigma$ -point. The blue polygon indicates the expected ranges for major avalanches according to the observations in Figure 8. Figure 9.b shows corresponding avalanche observations from major events. This has implication for the choice of model parameters as further discussed in the next section.

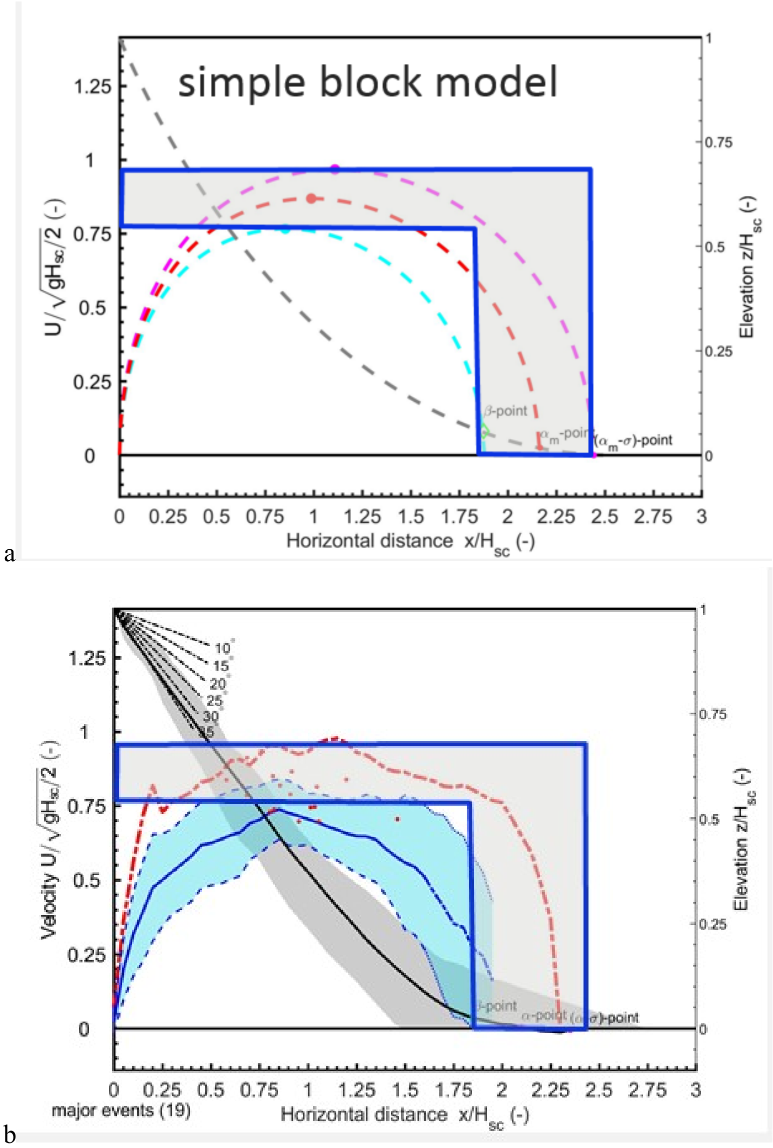

Figure 9 Scaling behavior of maximum front velocity of major avalanches combined with runout estimates. a) based on analytical calculations and b) corresponding avalanche observations from major events. The blue line shows the mean, the shaded area the ±σ-range and the red dashed line the observed maximum derived from observations along the track. The black line represents a "mean path" geometry and the gray shaded area the envelope of all path geometries.

Similarly, minor events show comparable behavior if the velocity is scaled by the actual drop height, H_{DH}, as shown in Figure 10.

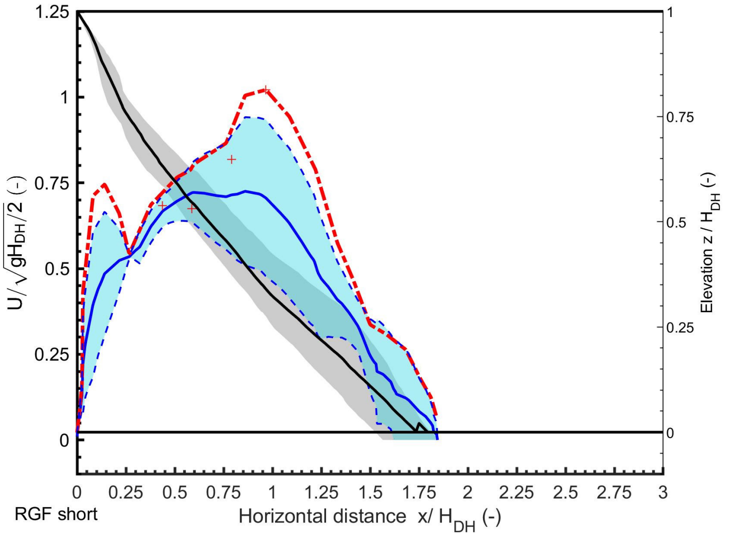

a)

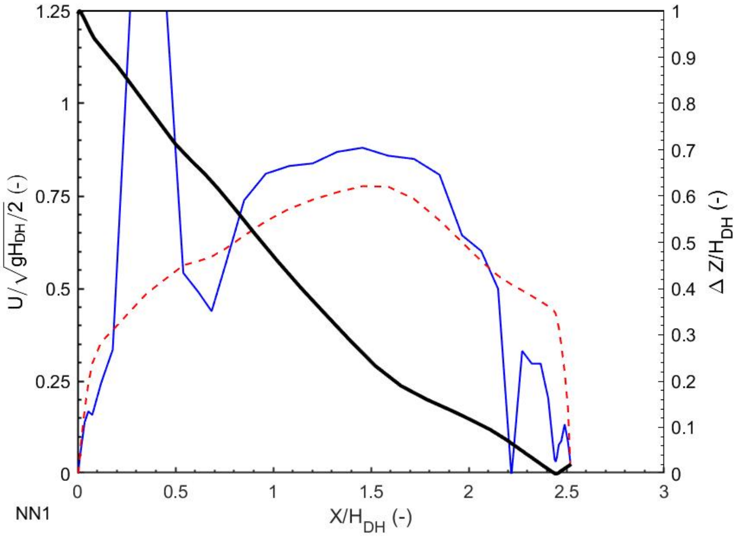

b)

Figure 10 Scaled avalanche velocity. a) Examples from avalanches at Ryggfonn (RGF)that stopped in the upper bowl ($H_{DH} \approx$300–500 m), b) avalanche accident in Tamokdalen, (Norway) on 2019-01-02; blue line shows the velocity derived from a GPS track and the red dashed line shows a corresponding model calculation with a simple mass block model using constant retarding acceleration ($H_{DH} \approx$200 m).

Cross-comparison of velocity simulations with measurements

As mentioned above, avalanche velocity is an important parameter to characterize the dynamic behavior. Observations imply that the maximum velocity of major avalanches scales with the total drop height H_{SC}, that is $U_{\max} \sim \sqrt{gH_{sc}/2}$ (McClung and Gauer, 2018; Gauer, 2018a; Gauer, 2014). Combined with estimates of the expected runout of major avalanches (e.g. Lied and Bakkehøi, 1980), these observations have implications for the choice of the empirical parameters of the Voellmy model that is used in most of present-day avalanche models.

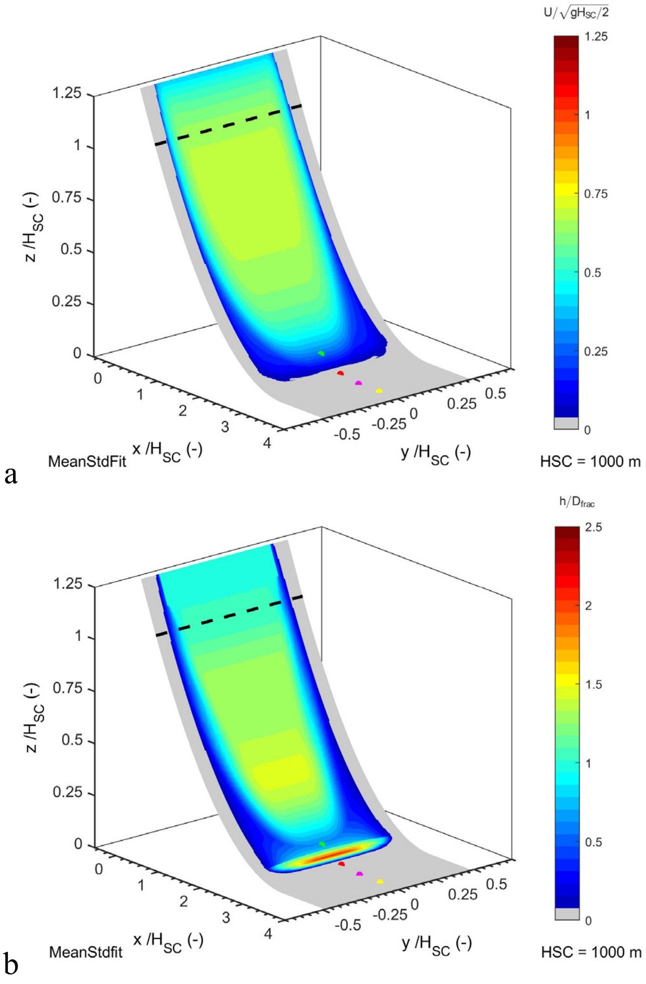

Figure 11 Test of RAMMS on parabolic tracks. a) Maximum velocity and b) maximum flow depth. The velocity is scaled as $U_{SC} = U_{max}/\sqrt{gH_{sc}/2}$ *and the flow depth as* $h = h_f/D_{frac}$*, where* D_{frac} *is the initial fracture depth.*

Using a simple parabolic track, model performance can be tested as shown in Figure 11 and Figure 12. Figure 12 shows a comparison of avalanche simulations with RAMMS (Christen et al., 2010) using the commercial version 1.7.20 for different drop heights. The volumes were adjusted according to expected deposition volumes. The corresponding release areas are located above the track, with an assumed fracture depth $D_{\mathrm{frac}} = 2$ m and a constant slope angle (in our case $\phi_0 = 35°$) given by the initial tangent of the track; the mean slope angle is $\beta \approx 23.8°$. The friction parameters are chosen according to standard values (Bartelt et al., 2017) corresponding to the respective volume class. However, only the highest elevation class is used, which gives the lowest friction values—that is, they should favor longer runouts and higher velocities.

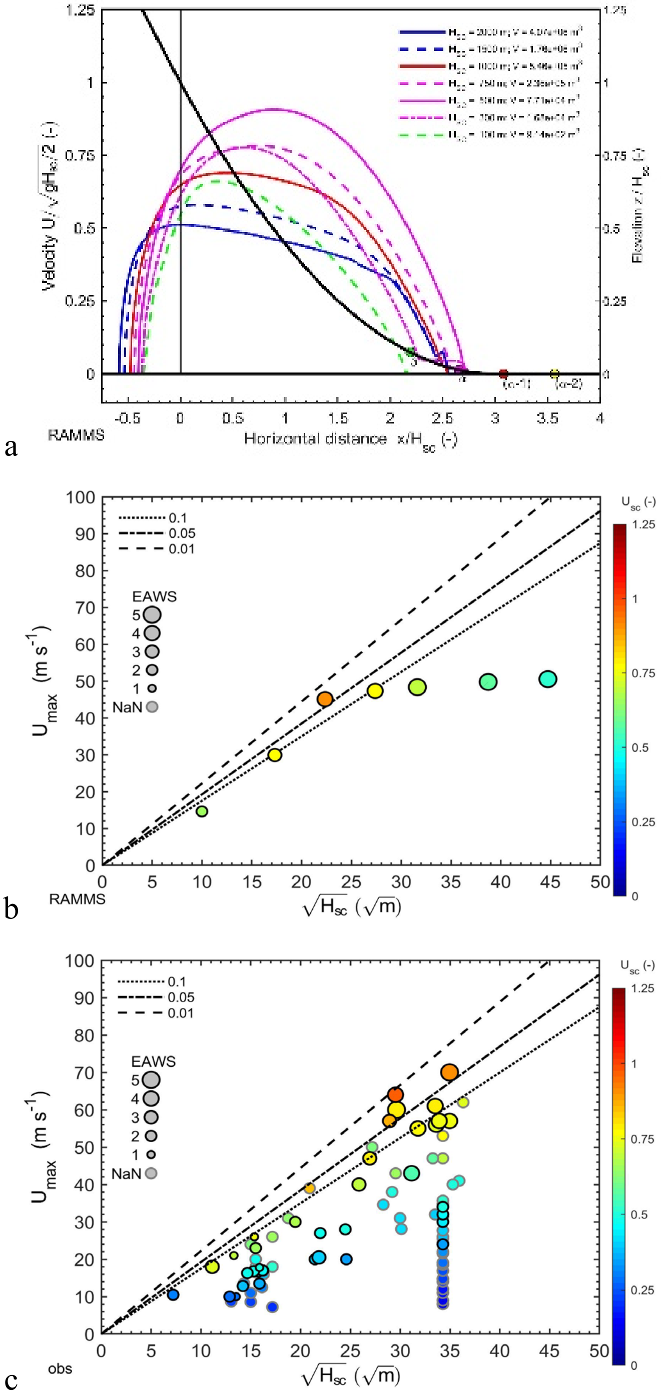

Figure 12 a) Simulated velocities with RAMMS along the thalweg for seven different drop heights. The release volumes are adjusted to the drop height and the fracture depth is set to 2 m. As a reference, the β, α, $\alpha-1\sigma$ and $\alpha-2\sigma$ points are shown (for an explanation see Lied and Bakkehøi, 1980). b) Simulated maximum velocity, U_{max}, versus square root of the drop height, $\sqrt{H_{sc}}$. The color illustrates the scaled velocity $U_{SC} = U_{max}/\sqrt{gH_{sc}/2}$ and the marker size corresponds to the EAWS avalanche size classes. The lines show the estimated exceedance probabilities derived from observations shown in panel c).

As can be seen in Figure 12a, the runout ends approximately at the mean expected α-angle according to the α-β model (Lied and Bakkehøi, 1980), even though the large assumed fracture volume would suggest that these simulations represent more extreme events. For drop heights up-to around 750 m, the simulated maximum velocities are in the range of rare events (cf. panels b and c). For drop heights above 750 m, the maximum velocity reaches a terminal velocity, which is not observed in reality. For drop heights larger than 1000 m, the simulations underestimate the velocities significantly compared to the observations. This is a typical problem for models based on the Voellmy-fluid rheology (see also discussions in Gauer, 2014, 2013, 2018a). However, also for drop heights smaller than 1000 m there seems to be a subtle difference as the simulated maximum velocity tends to be attained earlier in the path than observed in nature.

Figure 13 shows similar simulations for a drop height of 300 m and 1000 m, respectively, and varying mean slope angles, for which β is a good proxy. The simulated runout follows the expected mean α_m according to the α-β model. With increasing mean slope angle the simulated runouts tend to be longer than "expected". Also, the scaled maximum velocity tends to increase. However, it is obvious that the scaled velocity is lower for the cases with higher drop height.

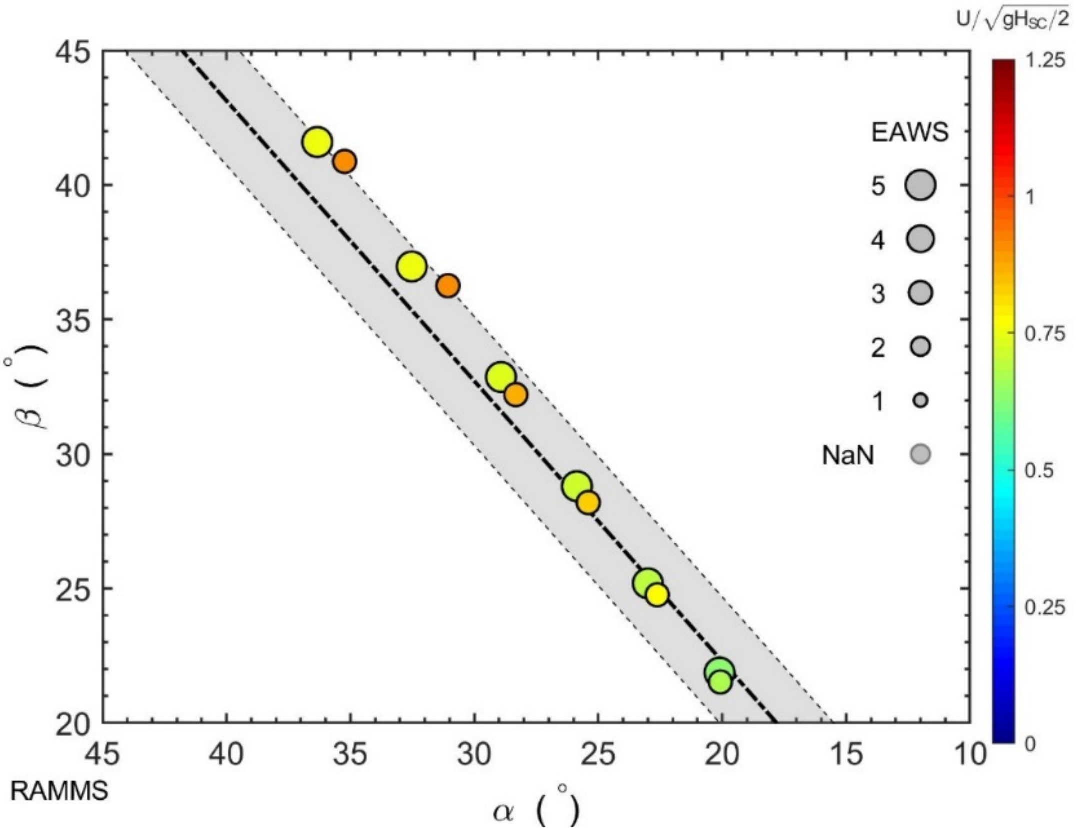

Figure 13 Simulated maximum velocities with RAMMS for a drop height of H_{SC} *= 300 m and* H_{SC} *= 1000 m (different sizes classes) and varying slope steepness. As a reference, the expected runouts according to the regression formula* $\alpha_m = 0.96\,\beta - 1.4^\circ$ *(black dashed-dotted line) and the ±σ range (gray shaded area) are shown (for explanation see Lied and Bakkehøi, 1980).*

Figure 14 shows a corresponding simulation with the code MoT-Voellmy under the same conditions as in Figure 11. The results are comparable to those from RAMMS but show some numerical artifacts.

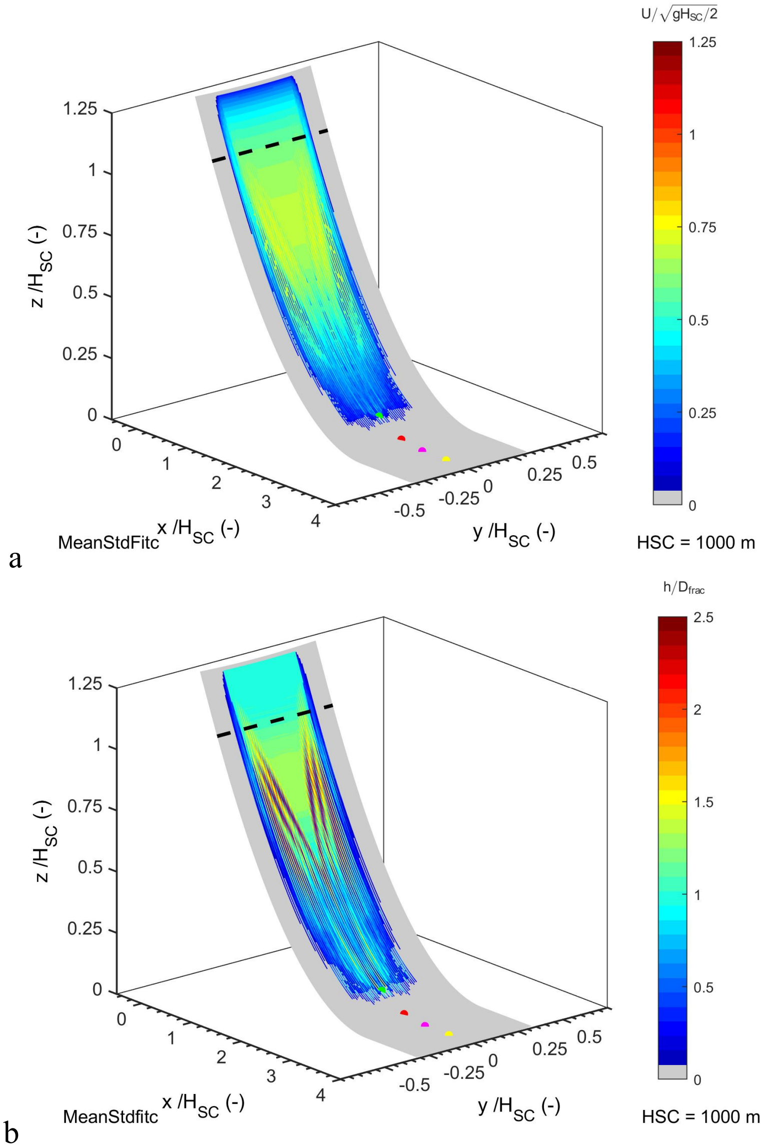

Figure 14 Test of MoT-Voellmy on parabolic tracks. a) Maximum velocity and b) maximum flow depth. The velocity is scaled by $U_{SC} = U_{max}/\sqrt{gH_{sc}/2}$ *and the flow depth by* $h = h_f/D_{frac}$*, where* D_{frac} *is the initial fracture depth (simulation to t = 100 s; build version MoT-Voellmy.2018-03-21.exe).*

Cross-comparison of the reach of the powder part of avalanches

In hazard mapping, practitioners are often required to assess the run-out distance and return period of dry-mixed avalanches—avalanches that are partially fluidized and accompanied by a powder cloud or air blast. The destructive effect of the suspension cloud or air blast can often be observed a considerable distance beyond the more easily discernible deposits of the dense part of those avalanches. At present, most avalanche models focus mainly on the prediction of the run-out distance of the dense- or fluidized part. In (Gauer, 2018b) estimates are presented that are based on a limited set of data from about 100 avalanche observations from Norway, Austria and Switzerland with drop heights of around 1000 m.

Figure 15 shows the observed excess runout of the suspension cloud quantified by $\Delta\alpha \equiv \alpha_{\mathrm{PSA}} - \alpha_{\mathrm{DF}}$ versus the β-angle (binned with a class width of 5°). The mean difference angle may by approximated by

$$\Delta\alpha = -0.17\beta + 3.1^\circ\,. \tag{2.5}$$

This implies that the expected relative runout increases for steeper tracks.

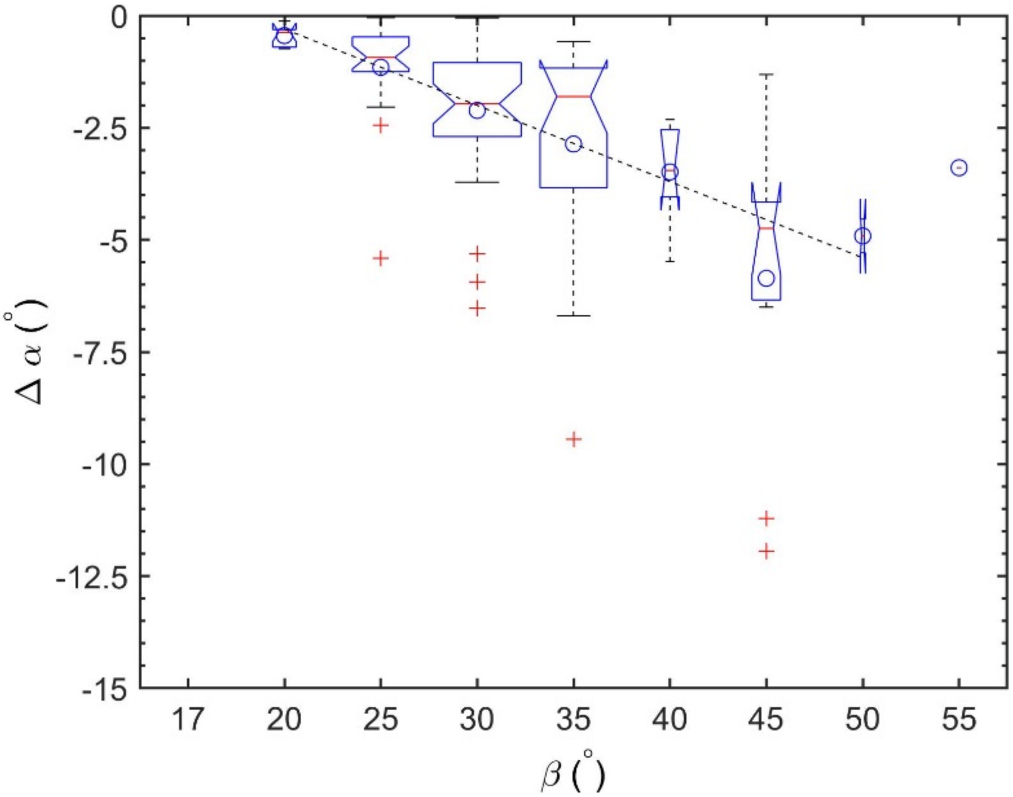

Figure 15 Estimates of the difference of the runout angle between the powder part and the dense part, $\Delta\alpha \equiv \alpha_{PSA} - \alpha_{DF}$, of dry mixed avalanches. The median is shown by the red central mark, the 25th–75th percentile as edges of the blue box, the whiskers extend to the most extreme data points not considered outliers, and outliers are marked by red crosses (points larger than $q_3 + 1.5(q_3 - q_1)$ or smaller than $q_1 - 1.5(q_3 - q_1)$, where q_1 and q_3 are the 25th and 75th percentiles). The notched area signifies a 95% confidence interval for the median, the mean is marked with a (o). The dashed line indicates the trend $\Delta\alpha$ vs β.

Cross-comparison of impact pressure on mast-like obstacles

The design of masts for electrical power lines, ski lifts, or cable cars in avalanche-prone terrain requires knowledge of the (impact) forces of snow avalanches on narrow obstacles. Recent observations show that avalanches, especially wet-snow ones, can cause large forces on this kind of obstacles (Gauer et al., 2008; Sovilla et al., 2010; Thibert et al., 2013; Ancey and Bain, 2015). Following the ansatz proposed in (Jóhannesson et al., 2009, Eq. (12.6)), the force on an obstacle can be expressed as

$$F_D \approx \rho C_{D0}\left(1+\frac{f_{CD}}{\mathrm{Fr}^2}\right) A \frac{U^2}{2} \tag{2.6}$$

where $\mathrm{Fr} \equiv U/\sqrt{gh}$ is the Froude number, U the velocity, h the flow height, A the projected area, and ρ is the avalanche density. The coefficient C^*_{D0} describes the effect due to the dynamic pressure and f_{CD} the additional contribution due to static pressure. Both coefficients may depend on the flow properties (in particular, the properties of the snow clods in the flow) and on the geometry of the obstacle. Figure 16 shows estimates of the combination of flow density and effective drag factor $C_D\ (= 2F_D/(\rho A\ U^2))$ based on observed impact pressures.

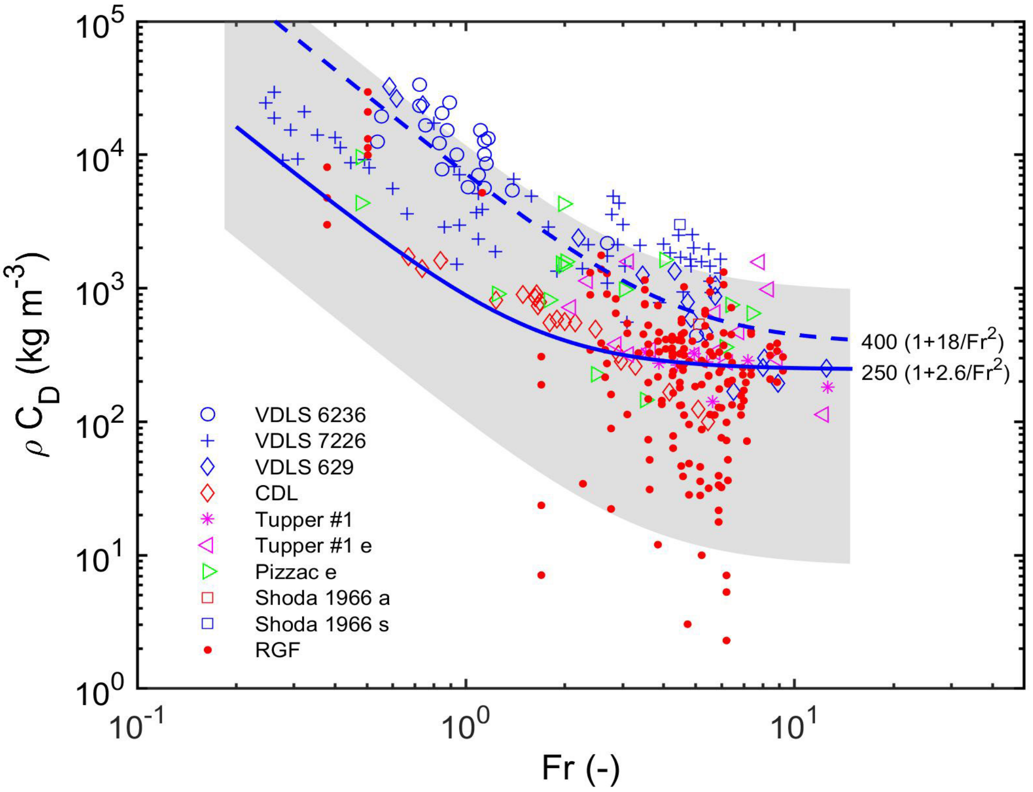

Figure 16 Estimates of the effective ρC_D vs. Froude number Fr $(= U/\sqrt{gh})$ based on measurements at various avalanche test-sites. The continuous line shows an upper limit (0.9 quantile) from measurements with load plates at Ryggfonn for dry-snow events; the dashed line shows a corresponding limit for wet-snow events. The gray shaded area indicates the quantile range between 0.1 and 0.9 for all measurements combined.

Forces on transmission line cables

There are few measurements of avalanche parameters above the dense/fluidized layer of an avalanche (above 4 to 6 m above ground). In the early years of the Ryggfonn test site, a transmission-line assembly was mounted across the lower part of the track, with three cables at heights of about 8 m, 12 m, and 16 m above ground. A limited set of data was obtained during that period, which provides some idea about the probable pressure distributions with height (Gauer and Kristensen, 2016). The observed pressures can be approximated by

$$p(z_{ai}) = C_D \rho_0 \frac{U_f^2}{2} \exp(-e_c z_{ai}) \qquad (2.7)$$

where e_c has the unit m^{-1} and depends on the velocity as

$$e_c = \max(0.583 - 0.0088 U_f, 0.05) \qquad (2.8)$$

Here, U_f is the front velocity, z_{ai} is the vertical height above the interface between the dense/fluidized layer and the powder part, ρ_0 is the avalanche density at this interface and C_D the drag factor for a power line ($C_D \approx 1$).

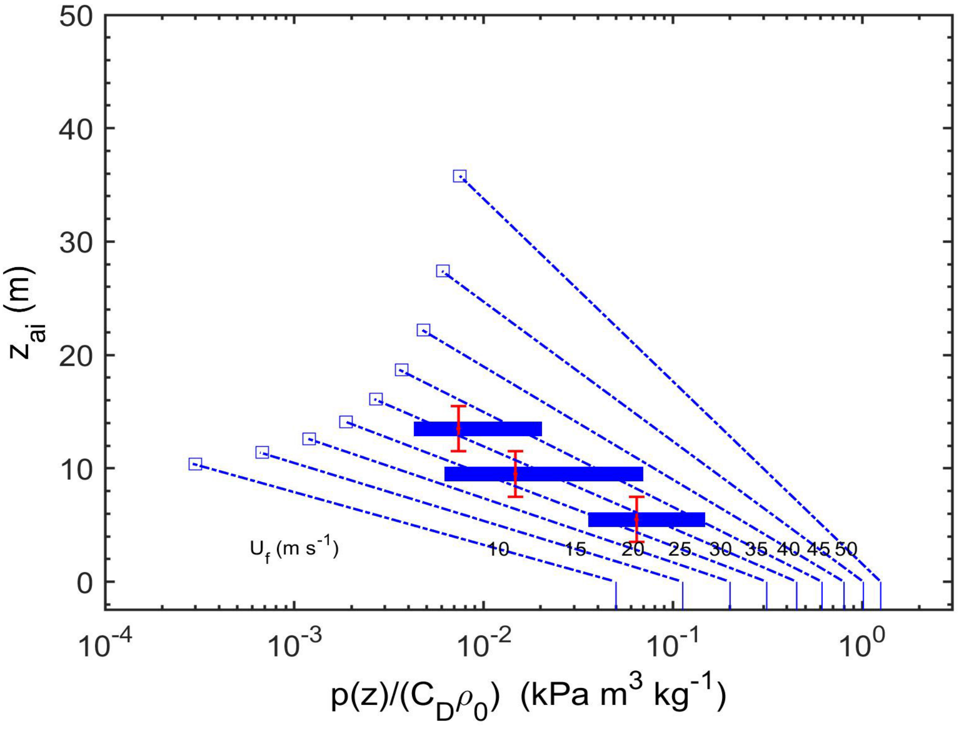

Figure 17 Estimates of the normalized pressure profile $p(z)/(\rho_0 C_D)$ based on measurements at Ryggfonn. The bars show the interquartile range of the measurements where the vertical lines indicate the median and the uncertainty range of the height. The dash-dotted lines show predictions according to Equation (2.8) with the front velocity U_f as parameter. The squares indicate the upper boundary of the powder part where the density has diminished and is close to the density of air. Note the log-scale of the abscissa.

2.3 Model development

Together with the publications (Grigorian and Ostroumov, 2020) and (Issler, 2020), this section constitutes Deliverable D1.6.

2.3.1 Avalanche–forest interaction

Contribution to friction and drag coefficients from trees

The measurements of the impact pressure on mast-like obstacles (Figure 16) provide also some indication of the braking effect of a standing forest (destruction of the forest is not considered). Considering again a simple block model (see Eq. (2.1)), Figure 18 shows how a forest would influence the parameters of a Voellmy-type model. The contribution due to the forest can be split in two parts. One is described by an enhanced Coulomb friction given by

$$\Delta\mu \approx d_t N_\perp \frac{C_{D0} f_{CD}}{2} h_f \, , \tag{2.9}$$

where d_t is the characteristic diameter of the trees, $N_\perp$ the number of trees per square meter projected (horizontal) area, and h_f is the flow depth. The other contribution is velocity-dependent and can be captured by modifying the parameter ξ (or, alternatively, the dimensionless parameter $k = g/\xi$):

$$\frac{1}{\xi} = \frac{1}{\xi_0} + \frac{1}{\xi_f} \quad \text{or} \quad k = k_0 + \Delta k \tag{2.10}$$

with

$$\frac{1}{\xi_f} \approx d_t N_\perp \cos\theta \frac{h_f}{g} \frac{C_{D0}}{2} \quad \text{or} \quad \Delta k \approx d_t N_\perp h_f \frac{C_{D0}}{2} \cos\theta . \tag{2.11}$$

Figure 18 shows how a forest would influence the parameters of a simple Voellmy-type model. The influence on parameters does not only depend on the forest stand alone, but also on the flow depth. This makes it difficult to include this effect in the available commercial Voellmy-type models. In contrast, these formulas are built into NGI's in-house code MoT-Voellmy.

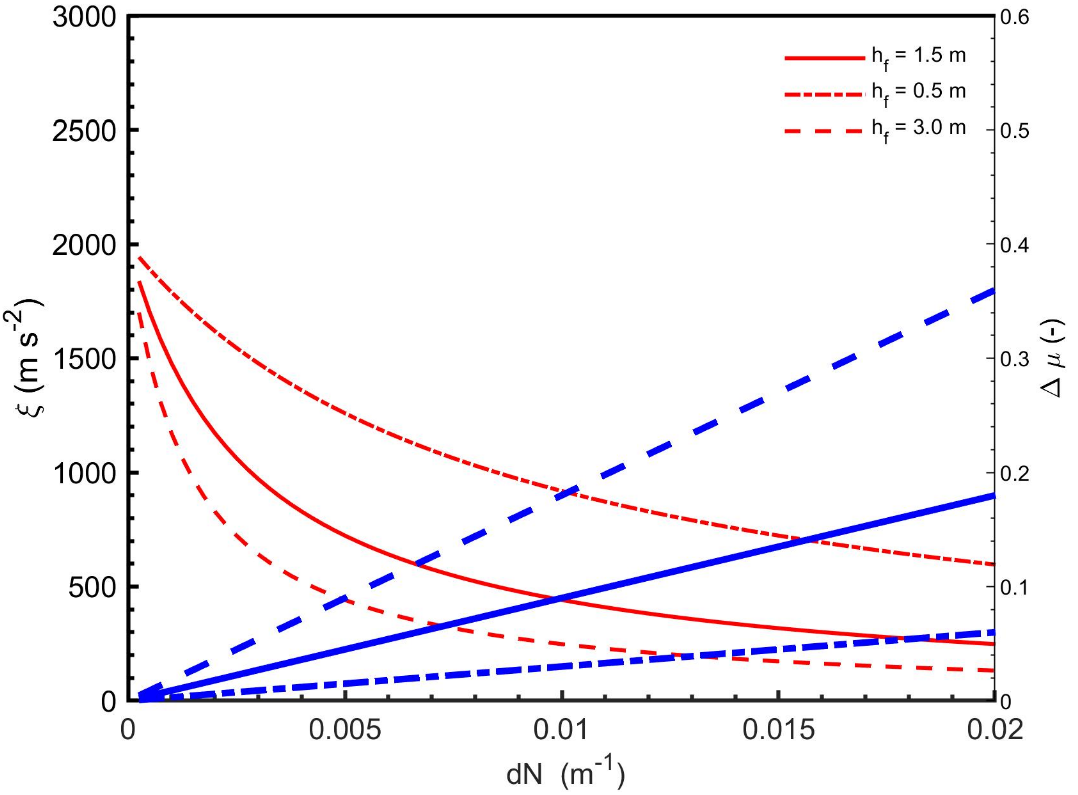

Figure 18 Braking effect of forest. Influence of the forest stand parameter dN on the parameters ξ (red) and $\Delta\mu$ (blue) of a Voellmy-type model with the avalanche flow depth h_f as parameter. ($\xi_0 = 2000$ m s^{-2} and $\Delta\mu = \mu_{\text{eff}} - \mu_0$)

Detrainment

Feistl and others (2012) as well as Teich and others (2014) hypothesize that forests extract mass from avalanches (detrainment), which causes them to stop in forests. They proposed to include detrainment in the mass balance as

$$\frac{\partial H}{\partial t} + \frac{\partial H U_x}{\partial x} + \frac{\partial H U_y}{\partial y} = Q_{e(x,y,t)} + Q_{d(x,y,t)} \tag{2.12}$$

where Q_e is the entrainment rate and Q_d the detrainment rate. For the detrainment rate, Feistl and others (2012) and Teich and others (2014) proposed the relation

$$Q_d = -\frac{K}{\rho|U|}, \tag{2.13}$$

where ρ is the density of the avalanche and $||\boldsymbol{U}||$ is the mean flow velocity. The parameter K accounts for mass detrained by different forest types per unit area and time. This relation suggests that mass will be detrained continuously if the avalanche passes a tree, which implicitly assumes that the storage capacity of a tree is unlimited. This is clearly not the case, as Figure 19 indicates. Therefore, the effect of detrainment can be severely overestimated by this approach, especially in the case of large avalanches. Furthermore, in the presented form Equation (2.13) suffers from a numerical singularity as $|U| \to 0$.

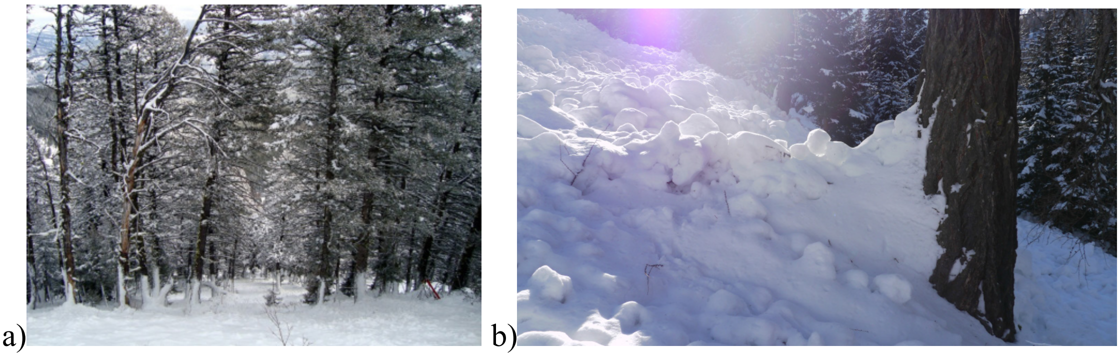

Figure 19 a) Traces of an avalanche running through a forest (photo Gallatin National Forest Avalanche Center, 2009-03-24). b) Deposition of avalanche snow in front of a tree (photo from (Feistl and others, 2012)).

Looking at Figure 19.b the order of magnitude of the deposition in front a tree can be approximated by a triangle (see Figure 20).

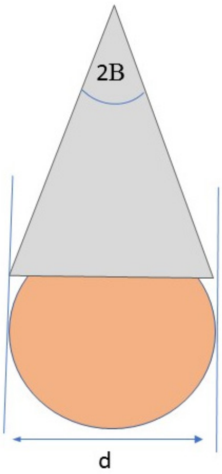

Figure 20 Sketch of snow deposition in front of tree stem after an avalanche has passed.

The volume deposited in front of a single tree can then be estimated by

$$V_{d0} \approx \frac{h_f d^2}{4 \tan B}, \tag{2.14}$$

where d is the tree diameter, h_f the flow height of the avalanche, and B is the opening angle. Regarding a forest stand on a slope with slope angle ϕ, the deposited volume per projected unit area is

$$\frac{V_d}{1\ \mathrm{m}^2} \approx \frac{N_{\mathrm{ph}\perp} \cos\varphi}{10^4\ \mathrm{m}^2} \frac{h_f d^2}{4 \tan B}, \tag{2.15}$$

where $N_{\mathrm{ph}\perp}$ is the number of trees per hectare projected (horizontal) area. That means, assuming a forest stand with $N_{\mathrm{ph}\perp} = 300/\mathrm{ha}$ and a mean trunk diameter of 0.5 m on a 30°

steep slope and assuming $2B \approx 45°$ and $h_f \approx 1.5$ m, 1 ha of forest would detrain about 200 m^3 (corresponding approximately to an average deposit depth of 0.02 m).

In contrast, Equation (2.13) suggests that there is no direct link to the forest parameters, except through the empirical parameter K, and that the deposition depth per square meter is proportional to the inverse of the avalanche velocity squared and proportional to the avalanche length.

Breaking and uprooting of trees – pressure and energy considerations

In the context of analyzing the field observations from the 2017 Rigopiano avalanche, which had destroyed a mature beech forest over 1 km (see Sec. 5.2.2), several questions arose: (i) Under which conditions can an avalanche destroy a forest? (ii) Will the trees be broken or uprooted? (iii) Is the avalanche capable of entraining the broken trees completely, or will it merely drag them along for some distance? (iv) How can forest destruction be implemented in avalanche flow models?

In (Issler, 2019b), the bending moment needed for breaking a tree trunk is calculated as

$$M_{b,\max} = \frac{\pi}{32} \mathrm{MoR}\, d^3 \approx (5\text{–}6)\ \mathrm{MPa}\, d^3\,, \qquad (2.16)$$

where d is the trunk diameter and MoR the modulus of rupture. The latter depends on the tree species and the water content of the wood; measured values in the literature have a considerable spread, but for beech one may assume MoR ~ 60 MPa. A dry-snow avalanche may be modeled as a cohesionless granular flow; experimental measurements of the drag of a long cylindrical obstacle can be well approximated by

$$p \approx \frac{C_D(\mathrm{Fr})}{2} \rho_f u_f^2\,, \qquad (2.17)$$

where p is the averaged pressure on the cylinder, ρ_f and u_f the depth-averaged flow density and velocity, respectively. The drag coefficient, C_D, which depends on the Reynolds number in a Newtonian fluid, is a function of the Froude number, given by $\mathrm{Fr} = u_f/\sqrt{h_f g \cos\theta}$. For a cylinder, it can be approximated as (Chehata et al., 2003)

$$C_D(\mathrm{Fr}) \approx 1 + 5\,\mathrm{Fr}^{-2}\,. \qquad (2.18)$$

Note that this formula does not apply to wet-snow avalanches, which will not be considered here.

The bending moment exerted by an avalanche flowing with velocity u_f and flow depth h_f on a slope inclined at the angle θ and covered by snow with depth h_s is

$$M_b \approx \frac{f(h_s/h_f)}{2} \rho_f (u_f \cos\theta)^2 h_f^2 d\,. \qquad (2.19)$$

The coefficient f accounts for the (unknown) velocity profile of the avalanche flow; it varies from $h_s/h_f + 1/2$ for a uniform velocity profile to $(4h_s)/(3h_f) + 1$ for a linear profile. This formula gives the bending moment at the base of the trunk; setting $h_s = 0$ results in M_b at the base of the flow. Assuming MoR ~ 60 MPa and typical values Fr =

3–7, $h_s/h_f = 0.3$–0.5, the minimum stagnation pressure $p_{\mathrm{stag}} = (1/2)\,\rho_f u_f^2$ for breaking trees is found as

$$p_{\mathrm{stag}} > (3\text{–}10)\ \mathrm{MPa}\ \frac{d^2}{h_f^2}. \tag{2.20}$$

For example, in an avalanche with $h_f = 2$ m, young trees with $d = 0.2$ m will break at stagnation pressures of 30–100 kPa, whereas mature trees with $d = 0.4$ m may resist up to 70–200 kPa. Such pressures are easily reached in large avalanches like the 2017 event at Rigopiano; the destruction of the forest along the path of the Rigopiano avalanche is thus not surprising.

The condition for uprooting is that the bending moment from the avalanche be larger than the resisting moment from the root system but less than the value needed for breaking the tree. Assuming a hemi-spherical root system of diameter D and a mean shear strength τ_r of the soil with roots, a tree can sustain a maximum bending moment

$$M_{r,\max} = \frac{\pi^2}{16}\,\tau_r D^3 \tag{2.21}$$

before being uprooted. Uprooting rather than breaking occurs if

$$\tau_r < \frac{1}{2\pi}\,\mathrm{MoR}\left(\frac{d}{D}\right)^3. \tag{2.22}$$

According to the literature, typical sizes of root systems are $D = (5$–$7)\,d$ in dense forest stands. This indicates 30 kPa $< \tau_r <$ 80 kPa in the case of the Rigopiano path. This range appears plausible for that path with karstic, highly fractured limestone bedrock and thin topsoil, but direct measurements are lacking.

There are several reasons why deducing similar bounds for powder-snow avalanches (PSAs) will be much more difficult: (i) The velocity, density and turbulence profile in PSAs are poorly known. (ii) The vertical flow structure at the front implies strong upward flow. (iii) PSAs are as high or higher than trees, hence the vertical profiles of the MoR and the effective exposed surface (which depends on the tree species and the density of the stand) will enter the calculation.

Does the forest destruction occur at the avalanche front or in the avalanche body? How long does it take for an avalanche to uproot or break a tree? These are decisive questions when it comes to estimating the degree to which forest destruction reduces the braking effect and to improving the simple approach (2.9)–(2.11). From the experiments and analysis of Dorren and Berger (2005), the work done by rocks fracturing trees can be approximated as

$$W_f \approx 0.03\ \mathrm{m}^{0.7} \cdot \mathrm{MoR} \cdot d_{\mathrm{BH}}^{2.3}, \tag{2.23}$$

with d_{BH} the breast-height diameter of the tree. Typical values for beech trees with $d_{\mathrm{BH}} = 0.2$–0.4 m are $W_f = 40$–200 kJ, similar to the values obtained in pulling tests. Depending on the breaking strength of the tree and the avalanche size, the fluidized front may or may not be capable of breaking the trees. However, if the fluidized layer has low pressure, it will in most cases be relatively small so that the dense flow arrives soon afterwards. This implies that in most cases, trees will begin to break or be uprooted very shortly after they are first hit by the avalanche.

2.3.2 Erosion and entrainment modeling

In contrast to most entrainment models for gravity mass flows that have been proposed in the literature (see (Eglit and Demidov, 2005) for a succinct review), there are three relatively simple ones that are based on general physical considerations and do not contain any freely adjustable parameters beyond material properties of the snow cover that are (in principle) measurable.

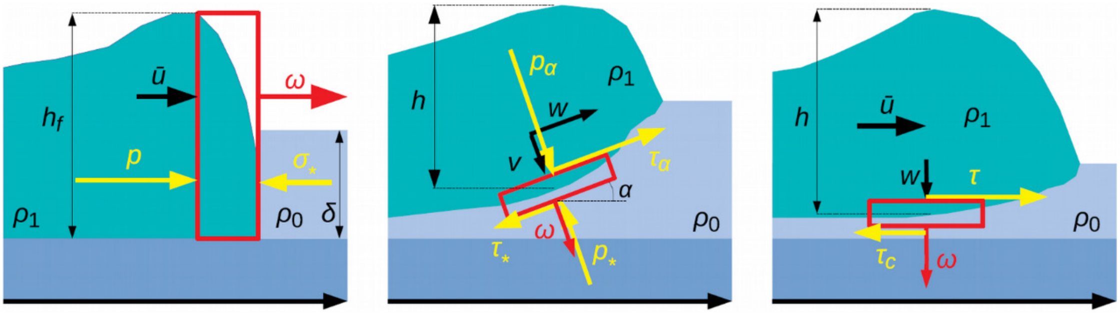

Figure 21 Control volumes (red boxes) used in the derivation of three different entrainment models based on shock theory. ***Left:*** *Eglit–Grigorian–Yakimov model for frontal (plowing) entrainment.* ***Middle:*** *Grigorian–Ostroumov model for basal erosion.* ***Right:*** *Tangential-jump entrainment model for basal entrainment. From (Issler, 2020).*

The oldest among these is the Eglit–Grigorian–Yakimov entrainment model (EGYEM) model for frontal entrainment (Briukhanov et al., 1967). It considers the avalanche front as a shock where the density, velocity and flow depth change abruptly (Figure 21, left panel). Frontal entrainment can sometimes be observed visually in slow-moving wet-snow avalanches that plow the snow cover ahead of them. The (hydrostatic) pressure exerted by the avalanche body must overcome the strength of the erodible snow layer, compress it and accelerate it to the speed of the avalanche. The shock propagates at a higher speed than the avalanching mass just behind it. A full mathematical description of this process would invoke jump conditions for the mass, the momentum and the energy across the shock to determine both the degree of snow compression and the propagation velocity of the shock. A simpler model with only the mass and momentum jump equations results if one assumes the flow density as given. This model has been implemented in the quasi-2D model MSU-1 and used extensively in the Soviet Union. Today, it would still provide the most realistic description of entrainment in wet-snow avalanches, but there does not seem to be any contemporary (quasi-3D) flow code that implements the EGYEM. One reason is that wet-snow avalanches are not usually considered explicitly in the models for avalanche flow, another is the need for exact front tracking, which is more involved in a quasi-3D model than in a quasi-2D one.

Another model is the Tangential-jump entrainment model (TJEM, Issler and Jóhannesson, 2011) for describing basal entrainment rather than frontal entrainment. The TJEM is also based on jump equations, but the infinitesimally thin control volume is oriented in the flow direction and parallel with the ground (Figure 21, right panel). Mainly the jump conditions for mass and for momentum in the flow direction, i.e., tangential to the control volume, are used. The difference between the shear stress exerted by the flow and the shear strength of the snow cover determines whether there is erosion or not and how large the entrainment rate is. As in the EGYEM, the density of the flow is assumed given. This model is implemented in NGI's numerical code MoT-Voellmy.

Already in the 1970s, Grigorian and Ostroumov (1977) applied the shock-front concept, not to the avalanche front but to the bottom of the avalanche, where the infinitesimally thin control volume is generally inclined at some angle $\alpha(x,t)$ with respect to the ground (Figure 21, middle panel). In contrast to the TJEM, the Grigorian–Ostroumov erosion model (GOEM) uses the jump conditions for mass and the interface-normal momentum component to derive an equation for the erosion rate. Again, the flow density is assumed given rather than computed from first principles.

No description of the model in English was available before a paper submitted by the authors to the Proceedings of a symposium in 1996, but that volume has never been published. Some work in this Work Package has been dedicated to careful editing and publication of the salvaged manuscript in a Special Issue on snow avalanche dynamics of *Geosciences* (Grigorian and Ostroumov, 2020) as well as a closer analysis of the GOEM and comparison with the EGYEM and TJEM (Issler, 2020). Some of the main results are briefly summarized here:

- The formulas for the erosion/entrainment rate can be cast into the same structure in all three models, namely

  EGYEM: $$q = \Theta(\bar{\sigma} h_f - \sigma_* \delta)\,\frac{\bar{\sigma} h_f - \sigma_* \delta}{u_f} \qquad (2.24)$$

  GOEM: $$q = \Theta(p_\alpha - p_*)\,\frac{p_\alpha(\bar{u}, h) - p_*}{v} \qquad (2.25)$$

  TJEM: $$q = \Theta(\tau_b - \tau_c)\,\frac{\tau_b(\bar{u}, h) - \tau_c}{\bar{u}} \qquad (2.26)$$

  See Figure 21 for the meaning of the symbols; $\bar{\sigma}$ is the depth-averaged hydrostatic pressure and given by $\bar{\sigma} = (h_f/2)\rho_1 g \cos\theta$ in terms of the slope angle θ.

- The models differ with respect to the relevant velocities (front velocity u_f for the EGYEM, interface-normal flow velocity v in the GOEM, depth-averaged flow velocity $\bar{u}$ in the TJEM) and the expressions for the stresses exerted by the flow and the strength of the snow cover.
- While the EGYEM and TJEM describe erosion (the destruction of the snow cover) *and* entrainment (the mixing of the eroded snow into the flow, the GOEM

strictly speaking only is concerned with erosion. To include entrainment, the jump condition for the momentum component parallel to the control volume would have to be included as well. The source term $-q\bar{u}$ in the depth-averaged equation of motion of the Grigorian–Ostroumov flow model, with q the erosion rate predicted by the GOEM and $\bar{u}(s,t)$ the depth-averaged velocity, enforces entrainment of the eroded mass without regard to consistency with the internal dynamics of the avalanche flow.

- In situations with $p_\alpha < p_*$ (GOEM) or $\tau_b < \tau_c$ (TJEM), the snow cover resists erosion, thus $q = 0$. In the EGYEM, however, $h_f\bar{\sigma} < h_s\sigma_*$ merely implies that the hydrostatic pressure from the avalanche is not sufficient to break the entire erodible snow layer. Eglit (1982) proposed three alternative extensions of the EGYEM to the case $h_f\bar{\sigma} < h_s\sigma_*$, but our analysis indicates that these options may need modification. A solution with a dynamically determined erosion depth in the range $0 \le h_e \le \delta$ has been found but needs careful checking and then testing by means of implementing it in a numerical code.
- Neither of the three models specify precisely how their measure of snow-cover strength (σ_* for the EGYEM, p_* for the GOEM, τ_c for the TJEM) is connected to measurable snow properties. An unequivocal measure of strength is the radius of Mohr's circle at failure (which corresponds to brittle fracture for snow impacted by an avalanche), which is the maximum shear stress in a plane inclined at 45° to the principal stress directions and which will be termed τ_* below. While measuring τ_* may be difficult under field conditions, it can in principle be done in the laboratory with a triaxial cell apparatus.
- If it is accepted that τ_* be used for characterizing the snow strength, the stresses $\bar{\sigma}$, p_α and τ_b can be transformed to the rotated coordinate system in which the shear stress is maximum, and then σ_*, p_* and τ_c can be replaced by τ_*. To carry out this transformation, some assumptions about the stress state of the snow cover need to be made: In the GOEM and TJEM, the deformations in the directions normal to the principal stress may be set to 0; the corresponding normal stresses can then be expressed in terms of the principal stress and Poisson's ratio. In the EGYEM, the deformation may be assumed zero in the transverse direction whereas the stress in the bed-normal direction depends on the depth. Some preliminary results are described in (Issler, 2020), but the problem needs some further work.
- In a typical snow pack in an avalanche-prone situation, there is a weak layer at the interface between the new and old snow or somewhere inside the old snow. The load and shear stress from an avalanche may therefore trigger failure in the weak layer even if the overlying layer does not fail. In such situations, step-wise erosion will occur, as hypothesized (Gauer and Issler, 2004) and observed experimentally (Sovilla et al., 2006). When this occurs, the avalanche flow is not able to accelerate the eroded snow to the mean avalanche velocity immediately but drags it along. Friction laws based on the depth-averaged flow velocity (like Voellmy's) may give substantially different bed shear stresses when applied to the average velocity of the fast upper layer or to that layer combined with the dragged layer. This question equally requires further study.

3 WP 2 – Statistical methods

3.1 Tests of StatPack in operational avalanche forecasting

StatPack has been used as an additional tool in avalanche forecasting at NGI since spring 2019. However, there is a significant drawback in the use of the alpha-beta relation for the estimation of runout probabilities as tests and discussions of the solution have shown. Therefore, only the avalanche triggering probability (ATP) is applied as support for the forecasting.

The main activities in WP2 have been to improve upon the newly developed StatPack model, test the model in avalanche forecasting, and guge its overall performance by comparing the model predictions with known snow avalanches. The latter task is the topic of a master's thesis at UiO, which is supervised through WP2.

The program package StatPack calculates the spatial distribution of the probability of a given point to be hit by a snow avalanche within the next 24 hours based on the weather conditions and the terrain. The focus in the master's thesis is testing of the StatPack model both by back-calculating eight known snow avalanches and by performing sensitivity tests on the ATP. The snow avalanches for the back-calculations have all a registered runout length including both the release and the runout area. An example from Tyinstølen in western Jotunheimen is shown in Figure 22. Extensive testing of the sensitivity of the different parameters that are involved in StatPack is also carried out. First, a set of typical weather situations characterized by a given set of parameters are determined. Then, for each weather situation one parameter at a time is changed and the effect on the ATP is found. In Figure 23 an example for the case from Tyinstølen shows how the ATP changes with changing snow height. The tests show remarkably low release probabilities as long as the probability of the presence of a weak layer is under 50%. The aim of testing StatPack in this thesis is to confirm and verify the performance of the model and try to find weather situations where the model struggles, and improvements must be made. The thesis will be submitted in June 2020, and final conclusions are not yet ready.

Some minor modifications of the model were made throughout 2019, mostly with to the goal of reducing the computation time. The model has e.g. been improved with faster interpolation routines (distribution of ATP factors depending on the terrain – direction and steepness). In addition, it is now possible to run the model without the runout part, i.e., the only output is the ATP at the defined release areas. The latter variant of StatPack is applied in operational forecasting. (This implementation and its integration in GIS was not funded by this project.)

There are several aspects in which further development of StatPack is both desirable and promising:

- Faster runout modelling, e.g.

  - by calculating the runout from a limited set of triggering cells, not all cells in a release area (make release areas sparse);
  - by precomputing runout distances: Multiply the probability of being hit along a slide path given a triggered avalanche by the ATP based on the actual snow conditions and weather situation.
- Distribution of the probability of being hit along the slide path. Now the calculation of this probability is based on the database of extreme events. The distribution must include shorter runouts as well. Work on the theoretical background is well underway, but not yet included in the model. See section 3.2 Runout probability
- Fix bugs as they are detected.

The model was developed in Python and the will be made available on the project web page as soon as the last adjustments are in place.

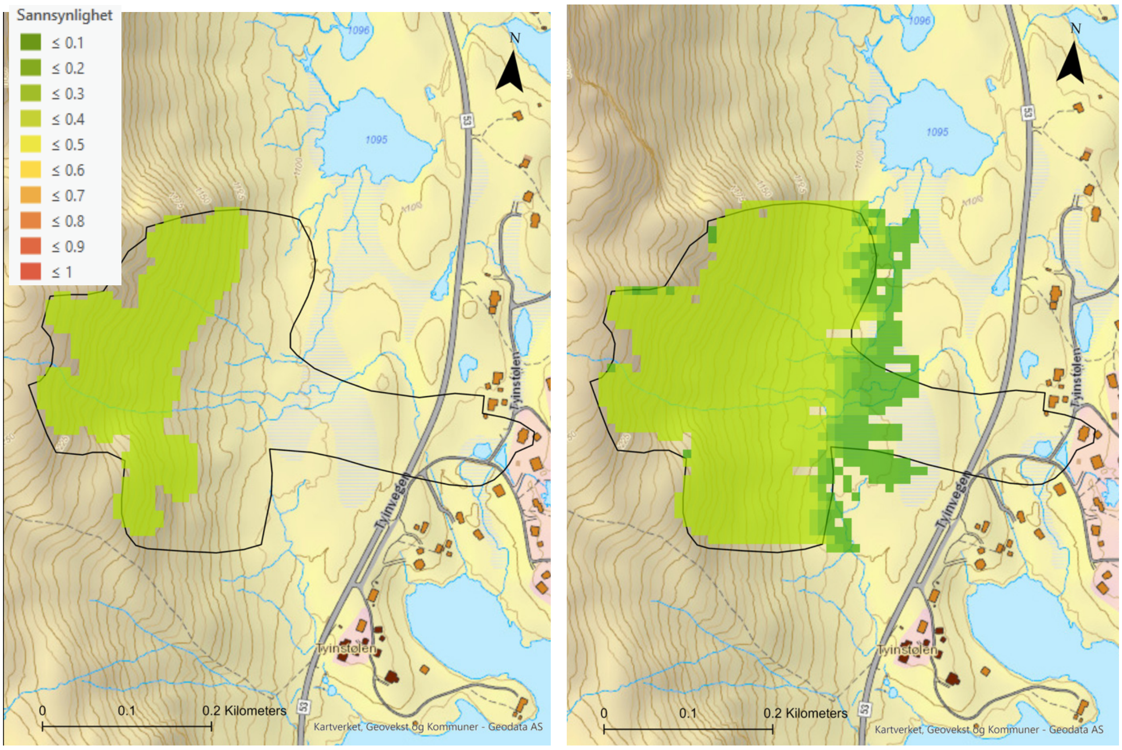

Figure 22: The avalanche triggering probability (left) and the probability of being hit (right) for a location at Tyinstølen, in the western part of Jotunheimen. The black line is the outskirt of an extreme avalanche event observed in 2008. The colour reflects the probabilities.

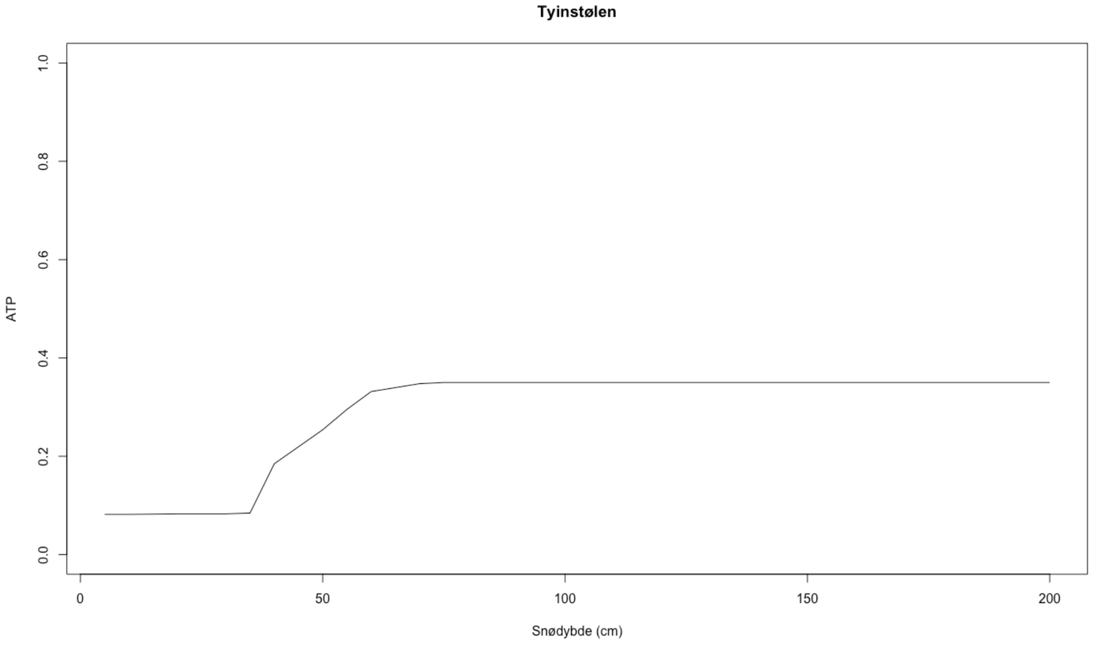

Figure 23: Change of ATP as a function of snow depth at Tyinstølen.

3.2 Runout probability

This section constitutes Deliverable D2.2.

For hazard assessments in a specific avalanche path, the probability distribution of the runout in space and time provides valuable information (McClung, 2000; Schläppy et al., 2014). However, to obtain this distribution a sufficiently long period with avalanche observations needs to be analyzed. Often, a complete set of runout observations is not available for the path in question and estimates are needed.

A first estimate may be obtained using some of the well-known statistical runout models like the α-β model (Lied and Bakkehøi, 1980) or the run-out ratio model (McClung et al., 1989). However, these models provide, strictly speaking, only estimates of the expected runout for a given single return period T_R (most likely of the order of 100 years).

To obtain some ideas about the annual runout probability at various positions s in a single track, one may write the annual probability P_a of the runout S to exceed the value s in the form (Schläppy et al., 2014; Serinaldi, 2014):

$$P_a(S > s) = \frac{1 - F(s|s \geq s_0)}{\bar{t}_0(s \geq s_0)}, \tag{3.1}$$

where S and s are travel distances along the track, $\bar{t}_0$ denotes the average inter-arrival time between two events exceeding the travel distance s_0, $F(s|s \geq s_0)$ is the cumulative distribution function (CDF) and $1 - F(s|s \geq s_0)$ is the (conditional) probability to observe a runout exceeding a specific value s with $s > s_0$. The average inter-arrival time can be approximated by

$$\bar{t}_0 \approx \frac{T_{\text{yr}}}{\text{NoA}}, \tag{3.2}$$

where T_{yr} is the observation period in years and NoA is the corresponding number of observed avalanches.

To obtain an estimate of the CDF $F(s|s \geq s_0)$, the probability distributions of a series of observed mean retarding accelerations in several avalanche paths are analyzed. The mean retarding acceleration a_{ret} is defined as

$$\frac{a_{ret}}{g} = \frac{\Delta H}{S}, \tag{3.3}$$

where ΔH is the drop height, S the travel distance along the track and g the gravitational acceleration. Figure 24 shows an example of such an observation series.

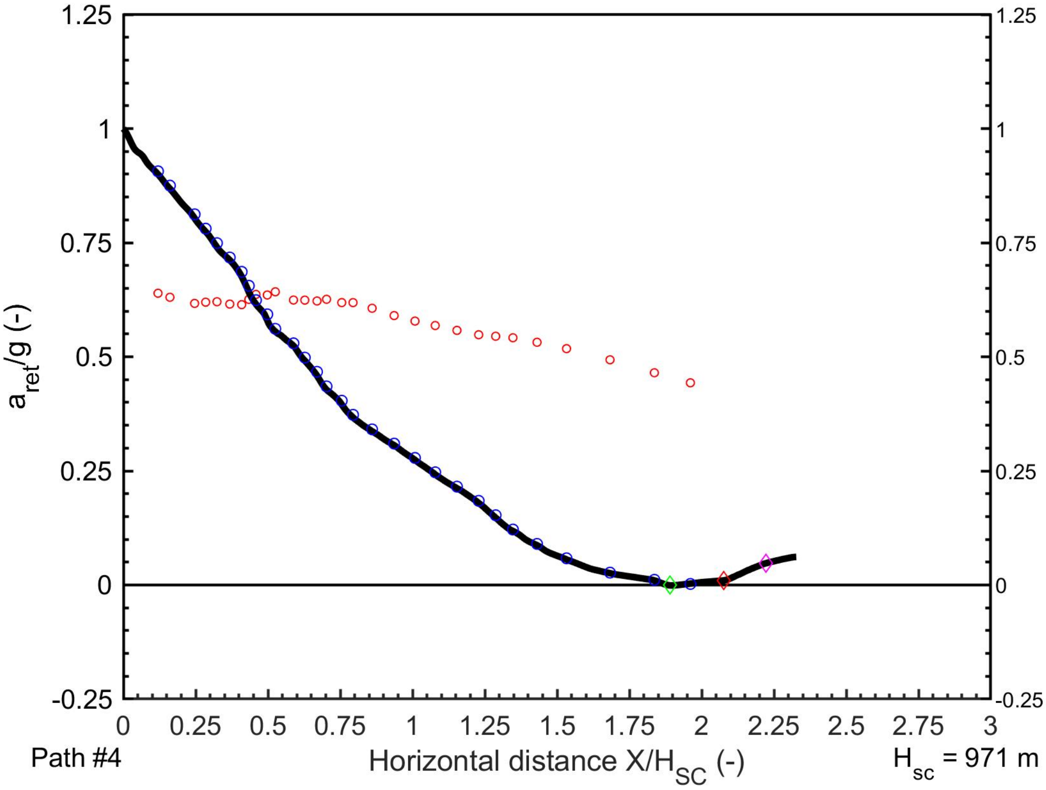

Figure 24 Example of runout observations (blue circles) and corresponding mean retarding accelerations a_{ret} (red circles). The diamonds mark the β, α and $\alpha - \sigma$ points (Lied and Bakkehøi, 1980).

In the following we focus on the normalized variable

$$\xi = -\frac{a_{\text{ret}} - M(a_{\text{ret}})}{M(a_{\text{ret}})}, \tag{3.4}$$

where $M(a_{\text{ret}})$ is the median of the observed a_{ret}. Figure 25 shows the survivor function (complementary cumulative distribution function, CCDF) of several series of observations and an overall fit assuming a Gumbel distribution with

$$r = \frac{\xi - \mu_G}{\beta_G}, \tag{3.5}$$

where μ_G is the location parameter and β_G the scale parameter, and the cumulative distribution function is

$$F(r) = \exp[-\exp(-r)]\,. \tag{3.6}$$

Using the quantile function

$$Q(p) = \mu_G - \beta_G \ln(-\ln p)\ ,, \tag{3.7}$$

one obtains an estimate of the retarding acceleration corresponding to a given probability

$$a_{\text{ret}}(p_{\text{ro}}) = M(a_{\text{ret}})\{1 + \beta_G[\ln(-\ln p_{\text{ro}}) - \ln(-\ln 0.5)]\}\,, \tag{3.8}$$

For a given annual probability $P_a(S > s)$, the corresponding runout probability P_{ro} is given by

$$P_{\text{ro}} = 1 - \bar{t}_0 P(S > s)\,, \tag{3.9}$$

where $0 < P_{\text{ro}} \leq 1$ is used. The probability P_{ro} of $M(a_{\text{ret}})$ is by definition 0.5.

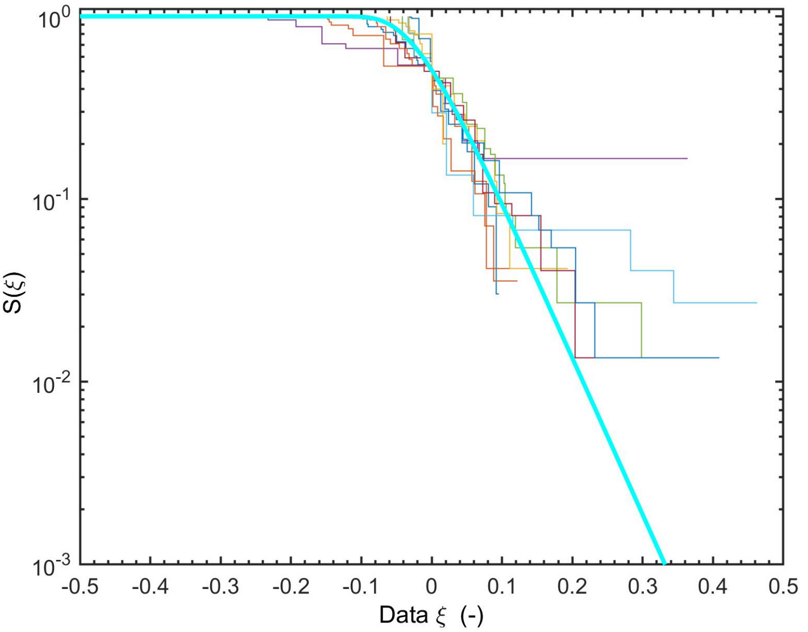

Figure 25 Survivor function (CCDF) of the observed ξ data. The cyan line shows a fit assuming a Gumbel distribution. Colors indicate different paths.

Figure 26 shows a Q-Q plot comparing the predicted values of a_{ret} versus the observed ones. The model based on a weighted mean value of the scale factor $\bar{\beta}_G$ of the Gumbel distribution provides reasonable predictions.

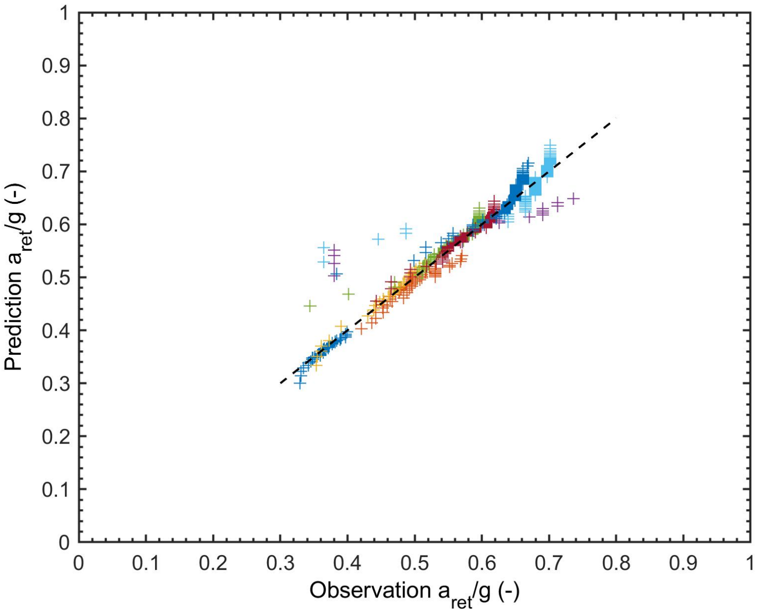

Figure 26 Prediction vs. observations (Q-Q plot) according to Eq. (3.8) using $\bar{\beta}_G \approx 0.051$*. The dashed line shows 1:1 plot. Colors indicate different paths.*

It should nevertheless be emphasized that the model cannot fully replace observations for a given path. To obtain estimates of the runout probability, it is at least necessary to have an estimate of one runout and its corresponding annual probability.

However, the presented approach might give some approximation of the ratio between two runout probabilities, for example:

$$\frac{a_{ret}(P_a)}{a_{ret}(0.1P_a)} \approx 1.15 \pm 0.1 \tag{3.10}$$

and

$$\frac{a_{ret}(P_a)}{a_{ret}(0.2P_a)} \approx 1.1 \pm 0.1\,. \tag{3.11}$$

To improve the model further, runout series in various avalanche tracks are desired. In addition, the statistical treatment might be improved.

4 WP 3 – Slushflows

4.1 Snow cover simulations

Existing snow cover models have problems to handle ponding water in the snow pack. The aim of this work package was to test the wet snow index (Mitterer and Schweizer, 2013) for its suitability for indication of slushflow situations where water can accumulate in the snowpack. Unfortunately, we did not manage to get the model SNOWPACK to work on our data due to large holes and periods with insufficient data coverage. In 2019, NGI has invested into a new weather observation system at Fonnbu that will give new possibilities in pursuing these questions.

4.2 Collection of observed slushflow velocities

Like for avalanches, velocity is an important parameter for characterizing the dynamic behavior of slushflows. Knowledge of velocity is, e.g., important for planning of mitigation measures. However, few measurements or observations are available and those that can be found in the literature are fraught with considerable uncertainties.

Table 4 and Figure 27 provide a small collection of published velocity observations of slushflows. Most observations originate from somewhere midways of the respective track, but still involve a considerable part of the total runout.

Table 4 Observations or estimates of (maximum) slushflow velocities

U ($m\ s^{-1}$)	Volume (m^3)	Total length (m)	Drop-height (m)	(Mean) slope angle (°)	Location	Date	Source
5±3	224	140	7	3	West Karakol Valley, southern Kirgiz Range, Kirgizstan	1992-05-16	(Elder, K. and Kattelmann, R., 1992)
20–30	6000	2800	300	7.5	Kvikkåa, Spitsbergen	1992-06-10	(Scherer et al., 1996)
24	104	1200	300	8-15	Kärkevagge, Sweden; 1st wave	1995-06-03	(Scherer et al., 1995)
38					Kärkevagge, Sweden; 2nd wave		
>20							(Gude and Scherer, 1998)
20–30	10^4	1500	400	15–20	Skarmodalen, Norway	2010-05-16	(NGI, 2015)
17				21	Holmatindi in Eskifjörður, Iceland	2019-02-23	priv comm. K. M. Hákonardóttir 2019; https://www.mbl.is/frettir/innlent/2019/02/23/krapaflod_a_eskifirdi/)
30		3900	1500	22	Mt. Fuji, Japan	2018-03-05	(Pérez-Guillén et al., 2019)

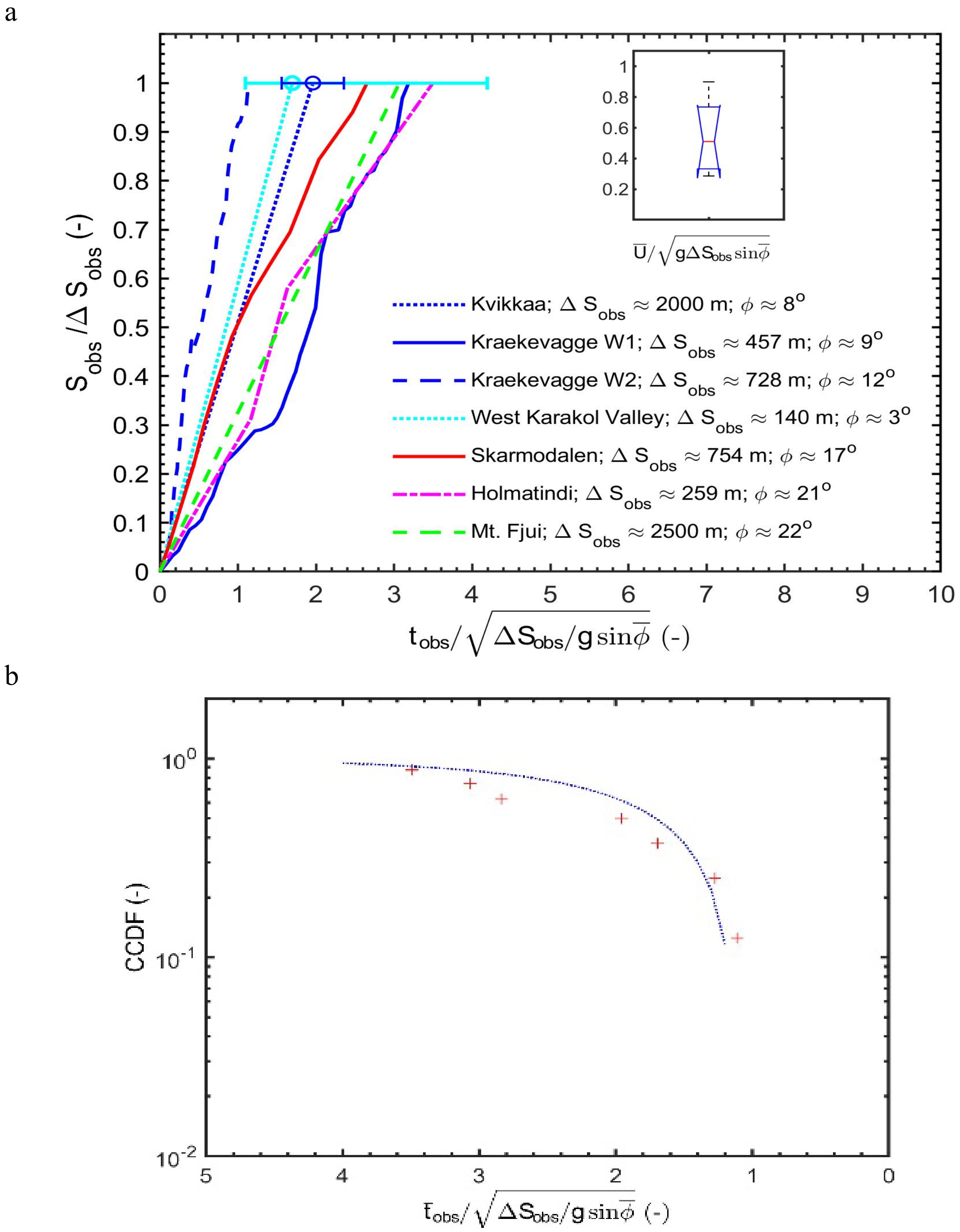

Figure 27 a) Observed slushflow mobilities expressed by the scaled travel distance $S_{obs}/\Delta S_{obs}$ vs. travel time $\bar{t}_{obs}/\sqrt{\Delta S_{obs}/g\,sin\,\bar{\varphi}}$, where ΔS_{obs} is the length of the observed stretch, $\bar{\varphi}$ the mean slope angle. The error-bars indicate the reported uncertainty ranges. The inlet shows a boxplot of the corresponding average velocity along the observed stretch scaled by $\sqrt{g\Delta S_{obs}\,sin\,\bar{\varphi}}$. b) Complementary cumulative distribution function (survival function) of the observed travel times $\bar{t}_{obs}/\sqrt{\Delta S_{obs}/g\,sin\,\bar{\varphi}}$.

4.3 Circum Arctic Slushflow Network

The Circum Artic Slushflow Network was pursued on a low level in 2019. The online literature list on the network's website was updated and the observation guidelines for slushflow events were established. The information is shared with members of the network. We also initiated a discussion on the best suited media for communication in the network. E-mail is obviously not the best way to share information and new observations. We will explore new ways of communicating interesting events within the network.

5 WP 4 – Avalanche observations

Sections 5.1 and 5.2 together with the reports and papers referred to therein constitute Deliverable D4.3. Section 5.3 together with the report (Gilbert, 2020) constitutes Deliverable D4.4.

5.1 Field observations of avalanche events in 2019

5.1.1 Avalanche at Blåbærtinden, Tamok Valley, Troms county on 2019-01-02

An avalanche accident at Blåbærtinden in the Tamok Valley in Troms county took the lives of four ski tourists on 2 January 2019. NGI assisted the rescuers during their difficult and prolonged work with assessments of the avalanche danger. During this work, several observations were made that could be analyzed in greater depth afterwards. The observations and subsequent analyses are summarized in (Sandersen, 2019).

Regarding avalanche research, the two most relevant observations concern the run-out distance and the speed of the avalanche. With a release volume of about 10,000 m^3, a total drop height of about 320 m and a run-out distance close to 660 m, it is a relatively small avalanche. Moreover, it is likely that this was not an extreme event for this path. Despite this, the avalanche exceeded the run-out predicted by the topographic-statistical α-β model by close to one standard deviation or about 100 m. This corroborates earlier incidental observations that this model may significantly underestimate the run-out of relatively small avalanches in areas with continental climate. It may be necessary to calibrate the model separately for areas with continental climate, but this can be done only if a sufficient number of avalanche paths with observations of quasi-extreme events can be found.

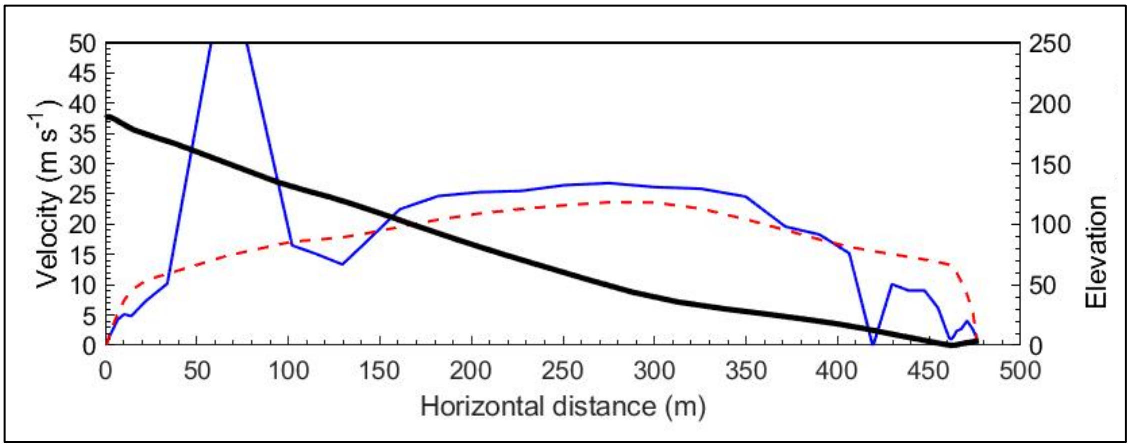

Figure 28 Avalanche speed as estimated by a dynamical model (red dashed line) and as inferred from GPS records extracted from the wristwatch/heartbeat monitor of one of the victims (blue line). The full black line represents the terrain profile and shows that the victims were transported by the avalanche over a drop height of about 200 m. From (Sandersen, 2019).

Interestingly, the observed run-out could be matched well by a simulation with RAMMS:AVALANCHE that assumed a fracture depth of 1.0 m (in agreement with the estimate from the survey) and friction parameters recommended for small high-altitude avalanches with a return period of 100 years. The simulations predict a peak velocity of close to 25 m s^{-1} and velocities above 20 m s^{-1} in the middle third of the trajectory (Figure 28).

One of the victims had a wristwatch with heartbeat monitor and GPS, which tracked not only the ascent of the touring group but also how the bearer was swept down the slope by the avalanche about 200 m vertical and 480 m horizontal. This data could be read out and allowed the velocity of the victim to be calculated. For the middle 300 m, the obtained velocities are in very good agreement with the numerical simulation.

5.1.2 Grandefonna powder-snow avalanche, Geiranger, Stranda municipality, Møre og Romsdal county on 2019-01-17

The Grandefonna is one of several well-known avalanche paths that threaten Geiranger— one of the prime tourist destinations in the Norwegian fjords, located at the end of the picturesque, narrow Geiranger Fjord. It released on 2019-01-17 as a mixed-snow avalanche (Figures Figure 29 and Figure 30) and closed the road between the village and the hamlet on Grandeneset for almost a week. This happened after a period with strong snowfall from NW (0.7–1 m of snow within three to five days) onto a thin old snow cover. According to the locals, this was the largest event in this path in the past 40 years. H. Breien surveyed the area on 2019-01-25; on 2019-01-30, the avalanche released again, without preceding precipitation but after a period with strong winds from NE.

Figure 29 Photo of the approaching powder-snow cloud of the Grandefonna avalanche on 2019-01-17. Photo taken by Sander Mossberg Hjelle, reproduced with permission.

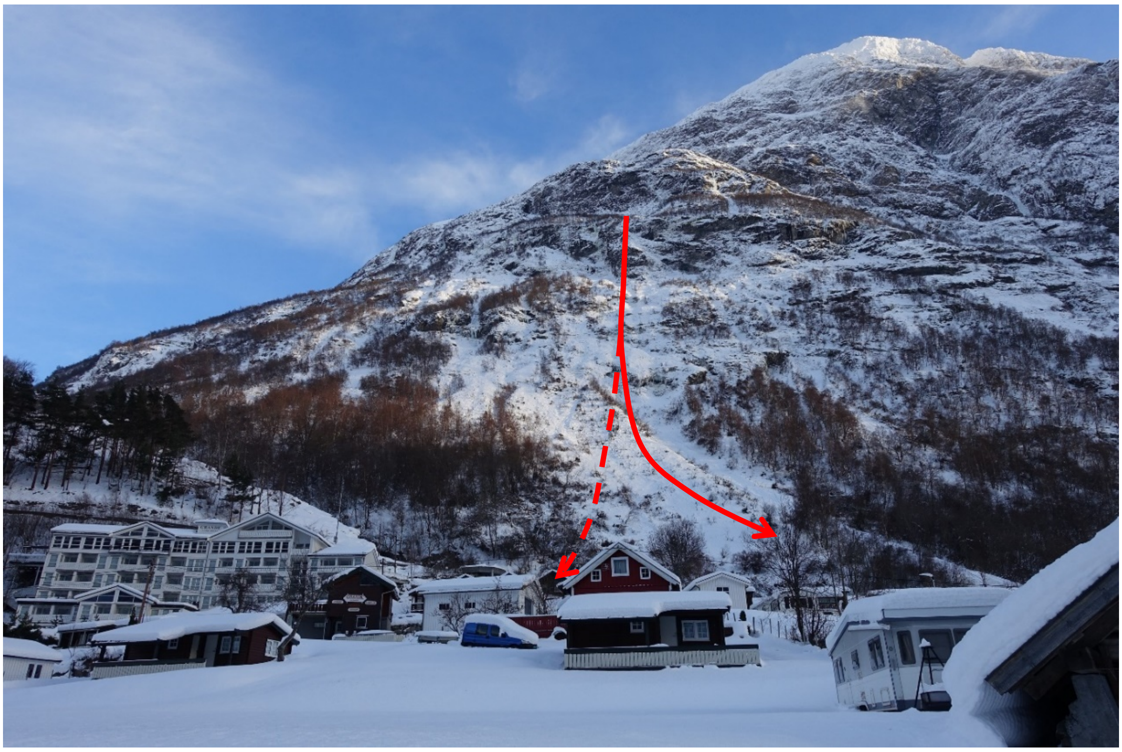

Figure 30 View of the Grandefonna path from the camping on Grandeneset. The release area is not known, but the avalanche presumably flowed as indicated by the red arrows. The powder-snow cloud proceeded in a straight line whereas the dense part followed the Grandhushammar gully. From (Breien, 2019).

The results of the survey are reported in (Breien, 2019). Further analysis of the pressure distribution in the powder-snow avalanche based on damage to the forest and absence of damage to the buildings on Grandeneset may be possible.

5.2 Analysis of earlier events

5.2.1 Powder-snow avalanches in Switzerland in January 1995

Two participants in the present project carried out field investigations of three avalanche events with widely different sizes from medium-size to very large in different parts of the Swiss Alps in January 1995. These three avalanches were special in that they provided an unusually clear distinction between three types of deposit in the same avalanche: One (type 1) consisted of snow blocks or rounded clods, had high density and was the deepest of the three. The second type consisted of round, hardened and compressed snow clods embedded in a fine matrix of small snow grains. It was found distally to, or to the sides of, the type-1 deposits where only the most mobile parts of the avalanche would be able to reach. It also had high density but was less deep than the type-1 deposits. Finally, the type-3 deposits consisted of small snow grains without embedded snow clods, with a somewhat lesser density than the type-2 deposits (Figure 31). They were found beyond the type-2 deposits, in one case extending over several kilometers. These observations provided very strong evidence for the occurrence of three different flow regimes in dry-snow avalanches, namely the dense-flow regime associated with the type-1 deposits, the powder-snow cloud producing the type-3 deposits, and in addition a regime of intermediate density at the front of such avalanches, which produces the type-2 deposits and is now termed the fluidized flow regime. Earlier experiments around the world had also obtained tell-tale signs of this intermediate flow regime, but for two decades it had not attracted due attention in the research community.

An internal report on the observations was published in German (Issler et al., 1996), but the need was felt to make these particularly clear observations accessible to the avalanche research community at large. In the meantime, experiments at Vallée de la Sionne in Switzerland and Ryggfonn in Norway had confirmed the inferences from these observations and yielded a deeper insight into the properties of the fluidized layer, but few if any practitioners take this knowledge into account in hazard mapping or when investigating avalanche events. Moreover, we found that the observations from 1995 could be analyzed in novel ways to give approximate mass balances for the different flow regimes, to distinguish to some degree between immediate and delayed entrainment of eroded snow, and to estimate the velocities, densities and pressure of the fluidized and powder-snow regimes at various points of the three paths. These analyses were published in a paper (Issler et al., 2020a), with additional information on the three events collected in the Supplementary Materials (Issler et al., 2020b).

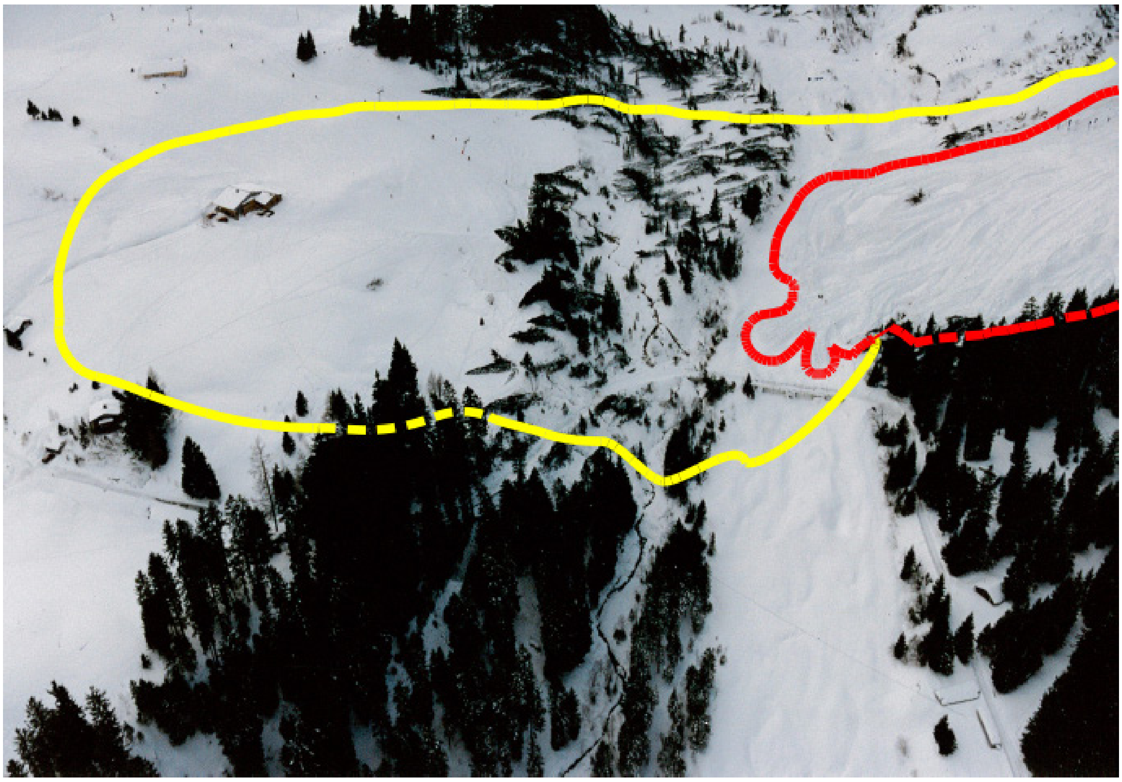

Figure 31 Aerial view of the run-out zone of the Albristhorn avalanche of 1995-01-30. The red and yellow outlines indicate the boundaries of the dense-flow (type 1) and fluidized-flow (type 2) deposits, respectively. The type-3 deposits from the powder-snow cloud could be traced some 500 m up the counterslope to the left. Photo S. Keller.

5.2.2 The Rigopiano avalanche, Farindola municipality, central Italy on 2017-01-18

The Rigopiano avalanche of 2017-01-18 was one of the most disastrous single avalanches in Europe in half a century, killing 29 persons waiting for their evacuation from a spa hotel that was completely destroyed by the avalanche. D. Issler had the occasion to visit the area (without access to the surroundings of the destroyed hotel, however) in June 2017 (Figure 32). Two reports on the observations, in particular the extensive damage to the forest, and their interpretation were finalized in early 2019 (Issler, 2019a,b). The latter will be modified for publication in a peer-reviewed journal in early 2020, with the former serving as supporting material.

It was found that trim lines in bends provide significant constraints on the velocity of both the dense and fluidized parts of the avalanche at several locations. They contain considerable uncertainties but are consistent with each other and similar inferences drawn from earlier observations in Switzerland (Issler et al., 2008). Setting up an approximate mass balance was difficult without access to further observational data like footage from drone flights, but it could nevertheless be concluded that the avalanche most likely eroded much more snow than it could fully incorporate into the flow.

Similarly, a large part of the trees that were broken or pulled out of the ground along about 1 km of the path were deposited again after they had been dragged over some distance.

Constraints on the avalanche pressure were obtained both from the damage to the forest and the destruction and displacement of the hotel. Again, the uncertainties are large, but all values appear consistent with each other and with the velocity estimates obtained from independent observational evidence. These values are also compatible with attempts at back-calculating this event with a numerical model (Frigo et al., 2018). In hindsight, it is not surprising that the avalanche destroyed a mature stand of beech over a length of 1 km. Moreover, energetic considerations suggest that the forest was destroyed by the frontal part of the avalanche.

These findings suggest the following conclusions, among others:

- Simple field observations, if analyzed with a view toward the dynamics of the avalanche, can often test whether our understanding of an event is adequate.
- Many avalanches erode the snow cover faster than they can entrain it, leading to a layer of eroded material that is dragged along by the flow. Erosion/-entrainment/deposition models that account for this erosion regime need to be developed.
- The forest resistance model implemented in MoT-Voellmy, which is probably one of the more advanced of its kind, assumes that the forest is not destroyed by the avalanche. This leads to a very substantial overestimate of the braking effect of a forest in medium-size and large avalanches. A more advanced forest-resistance model with a simple yet adequate breaking criterium and coupling to the erosion/deposition model should be developed.

Figure 32 View from the eastern slope of Monte Siella towards Rigopiano. the trim lines along the bends of the avalanche path and the tree debris spread along the centerline could be used to infer constraints on the flow velocity and the effectiveness of entrainment, respectively. Photo D. Issler.

5.3 Avalanche observations with infrasound and seismic sensors

This section, together with the report (Gilbert, 2020) and the paper (Pérez-Guillén et al., 2019), constitutes Deliverable D4.4.

Near-real-time information about avalanche activity in a region is of invaluable help for local avalanche forecasting. Knowing the avalanche activity in neighboring paths ("indicator avalanches") can be critical in understanding the current snow-stability conditions and for evaluating past bulletins (Kristensen 2016). Reliable systems for automatic monitoring of avalanche activity that can supplement visual observations are desirable for verification and operational forecasting.

The main technologies capable of such monitoring are (i) video recording, mainly from fixed locations, (ii) networks of seismometers, and (iii) infra-sound arrays. At the scale of single mountain sides, one can also use terrestrial LiDAR scanning, Doppler RADAR and InSAR (Interferometric Synthetic Aperture RADAR). All these systems have their specific strengths and weaknesses, e.g., high spatial resolution and easy interpretation vs. dependence on sufficient light and contrast in the case of video recordings. Filtering out background noise with sufficient certainty and in near-real-time is a major challenge for seismic networks and infrasound arrays. Satellite-based remote sensing techniques are also capable of detecting avalanche activity over large areas (Eckerstorfer et al., 2014), but at present images of sufficient resolution are not available frequently enough for use in daily avalanche forecasting.

The main activity in this task during 2019 consisted of another season of measurements with the infrasound detection of avalanches (IDA) array in Grasdalen and the analysis of five seasons of operation. A small side activity was the publication of a study (briefly reported on in the Annual Report 2018) on seismic detection of snow avalanches and slushflows on Mt. Fuji, Japan.

5.3.1 Avalanche detection by infrasound in Grasdalen

As explained in earlier Annual Reports, an infrasound avalanche detection system (IDA) was installed in Grasdalen in October 2014 by the Norwegian Public Roads Administration (NPRA) in collaboration with Wyssen Norge AS to test the feasibility of continuous avalanche monitoring (Humstad et al. 2016). The IDA system is based on technology developed by iTem and Laboratorio di Geofisica Sperimentale of the University of Florence, Italy (Ulivieri et al. 2012). The NPRA had initially decided to discontinue the monitoring program in Grasdalen after the 2015–2016 season and to remove the infrasound detection system. Following a proposal from NGI to share the costs of operation, it was decided to continue the research program for two more seasons. During the winter 2017/2018, technical problems led to long periods of downtime. To make up for this, Wyssen Norge AS offered to leave the system operational in Grasdalen also in the winter 2018/2019 at no additional cost.

The IDA array was positioned in Grasdalen (Location 1, 61.9792° N, 7.2902° E) between autumn 2014 and spring 2017. From autumn 2017 to spring 2019, the IDA system was repositioned further up the valley near the entrance of the Oppljos tunnel (Location 2, 61.9925° N, 7.3146° E). The new location is more relevant to NGI's local forecasting operation and allows comparison with visual observations. Wyssen Norge AS modified the detection system with five new sensors, better sound isolation and improved GPS equipment. The array locations are marked in Figure 34.

The main criteria used in identifying avalanche signals are signal duration, peak amplitude, and thresholds related to the kinematics of the migration of the signal source (i.e. the avalanche). The infrasound waves produced by snow avalanches typically persist for 15 seconds or more and migrate over time. Avalanches can thereby be distinguished from explosions or background events, which are typically of shorter duration or originate from a static point. Processing of the infrasound data (filtering and classification) was done by Wyssen. Events were classified into three types—high reliability, low reliability, or explosions— based on the degree to which the criteria were met (Marchetti et al., 2015).

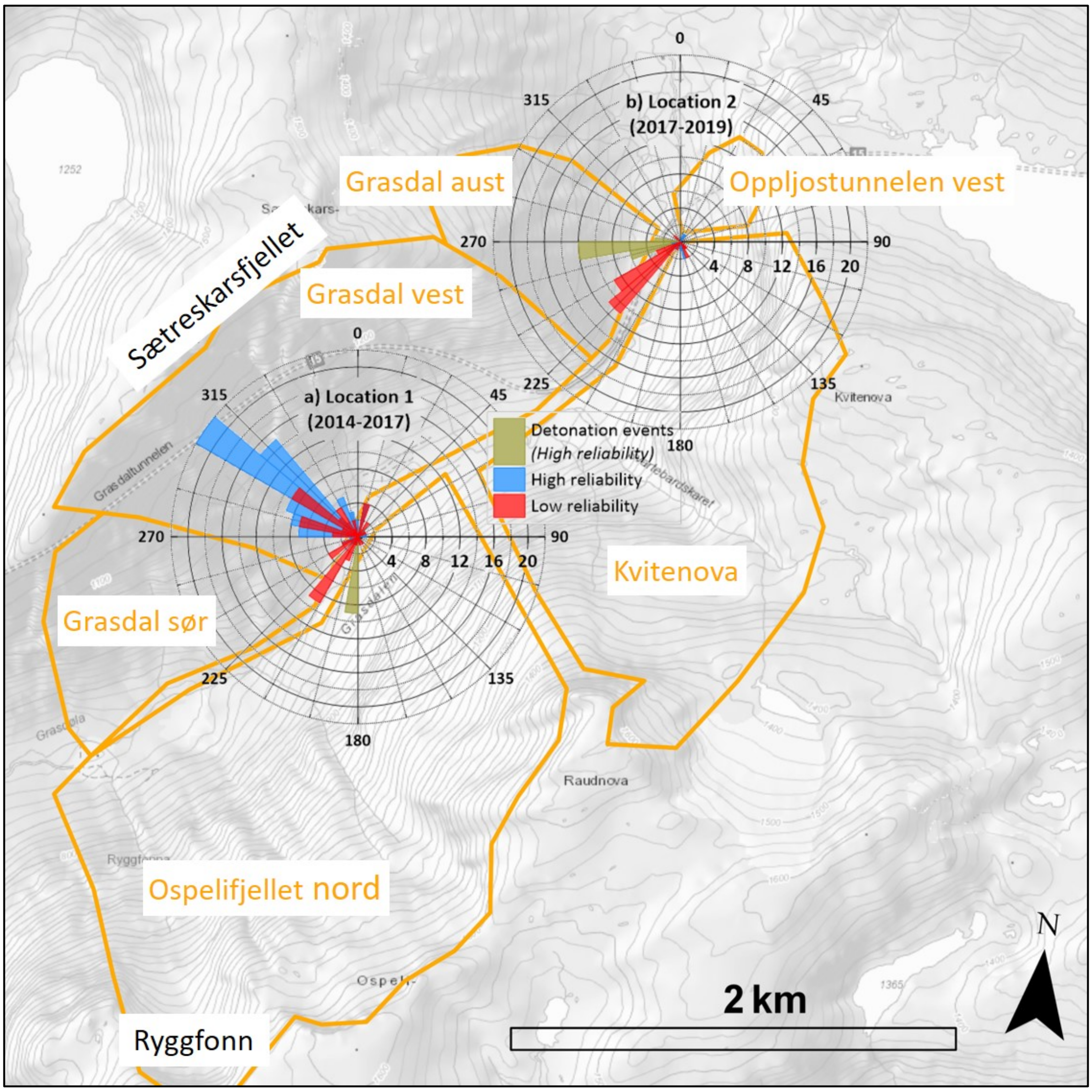

Figure 33 Infrasound monitoring locations in Grasdalen and back-azimuth directions for reported events.

57 high-reliability events and 55 low-reliability events were recorded while the station was positioned at location 1. High-reliability events originated mostly from Grasdal vest

(Sætreskarsfjellet). High- and low-reliability detections are from this direction are likely to be avalanches given the topography in the sector. It is less certain what factors are registering as low-reliability events along the valley axis. Possible agents may include distant avalanches or traffic noise. In addition, 13 explosions (avalanche control) were recorded on three separate days in the direction of the Ryggfonn test site. The timing matches with that of the Ryggfonn campaigns.

Following the repositioning of the array to location 2, the IDA system registered 11 high-reliability events (Fall 2017 to Spring 2019). The back-azimuth values from these events point to infrequent avalanches in the following areas: Grasdal aust, Oppljostunnelen vest, and Kvitenova. Low-reliability events (*N* = 29) commonly point towards the southwest and may be caused by smaller avalanches or traffic noise near the entrance to the Grasdal tunnel. 21 detonations were recorded. Detonations were due to avalanche control at Sætreskarsfjellet conducted by the NPRA, detonations at Ryggfonn were not detected at a distance of 4–5 km. Avalanches triggered by detonations were commonly confirmed by observations from NGI's automatic camera located near Fonnbu. Natural avalanches detected by the array frequently occurred during periods of low visibility either due to heavy snow fall, drift, or darkness. It was therefore not possible to confirm the high-reliability detections using this camera.

The infrasound array was not operational for a portion of the avalanche seasons between 2014 and 2016 (Humstad et al. 2016). It is unclear when the station was operational in the 2016–2019 period. This information should be included in an updated evaluation.

5.3.2 Seismic detection of avalanches at Mt. Fuji, Japan

In 2018, D. Issler contributed to a study on detection of snow avalanches and slushflows at Mt. Fuji, Japan during a research stay at the University of Nagoya. In that study, it was shown that a network of seismometers—mainly used for monitoring the ground tremors connected to volcanic activity—can detect, locate and track medium-size to large snow avalanches over distances up to 5–15 km by means of the so-called amplitude source location (ASL) method (Figure 34). The work was then presented at the International Snow Science Workshop (Pérez-Guillén et al., 2018). In 2019, an extended version of this work was published in a peer-reviewed journal (Pérez-Guillén et al., 2019).

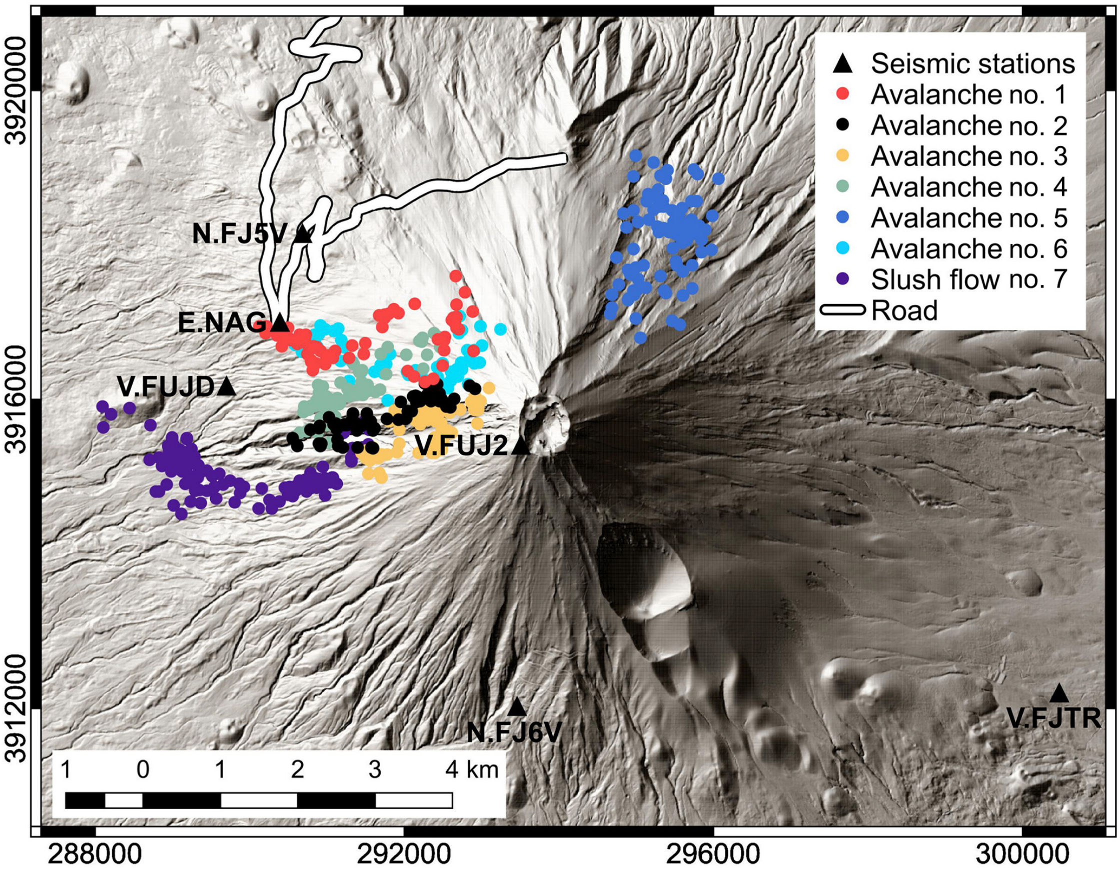

Figure 34 Map showing the seismic locations of the seven detected avalanche events on Mt. Fuji and six seismometers of the seismic network. From (Pérez-Guillén et al., 2019).

It appears feasible to improve the precision of avalanche location by suitable modification of the weighting of amplitudes from different sensors. The precision and reliability of flow velocity estimates based on seismic signals is fundamentally limited by the fact that the dominant seismic energy source need not be located at or near the avalanche front and may even be stationary. When it comes to monitoring of large areas, the cost and logistics of installing and maintaining many seismometers with real-time data transmission becomes a decisive factor that requires further study. The main challenge will, however, be the development of robust and efficient algorithms for detecting avalanche signals in the noise due to small earthquakes, traffic, etc.

6 WP 5 – Improved tools for local avalanche forecasting

Quantification of release probabilities in local avalanche forecasting are depending on knowledge of historical weather characteristics as well as detailed knowledge of the wind-driven snow distribution on a fine scale. In WP5 we have computed extreme weather statistics for snow and other related parameters for historical and future climates at 1 km^2 resolution, and prepared gridded regional scale wind data for use in statistics together with historical gridded data. Within each 1x1 km^2 grid cell wind is the dominant factor determining snow distribution in the terrain. Simple terrain indexes as well as a complex fluid dynamic (CFD) model have been tested and evaluated with respect to performance in modelling wind fields and determining snow distribution and potential release areas. Several scripts and tools have been developed along this study with the aim of establishing an improved toolbox for avalanche forecasting on a local scale.

6.1 Release areas determined by a simple terrain index

The Winstral sheltering index provides a quick overview of lee areas for a given wind direction. At Sæterskarsfjellet in Grasdalen avalanches are often released after precipitation and westerly to northwesterly winds. The SX-factor for 8 wind directions is derived from the same 10 m resolution DEM as used for the WindSim runs, and here shown for values above 0.6 (orange) and 0.7 (red). For westerly winds (270°) the highlighted potential release areas fit the major observed release areas well (Figure 35). For northwesterly winds, only release areas in the southern side of Sæterskarsfjellet are highlighted, even though we know that northwesterly winds can result in avalanches also along the ridge. Due to terrain effects on the wind field, wind may still come from westerly directions when the main wind direction is northwesterly. To account for these effects, we therefore need physical representation of the wind field.

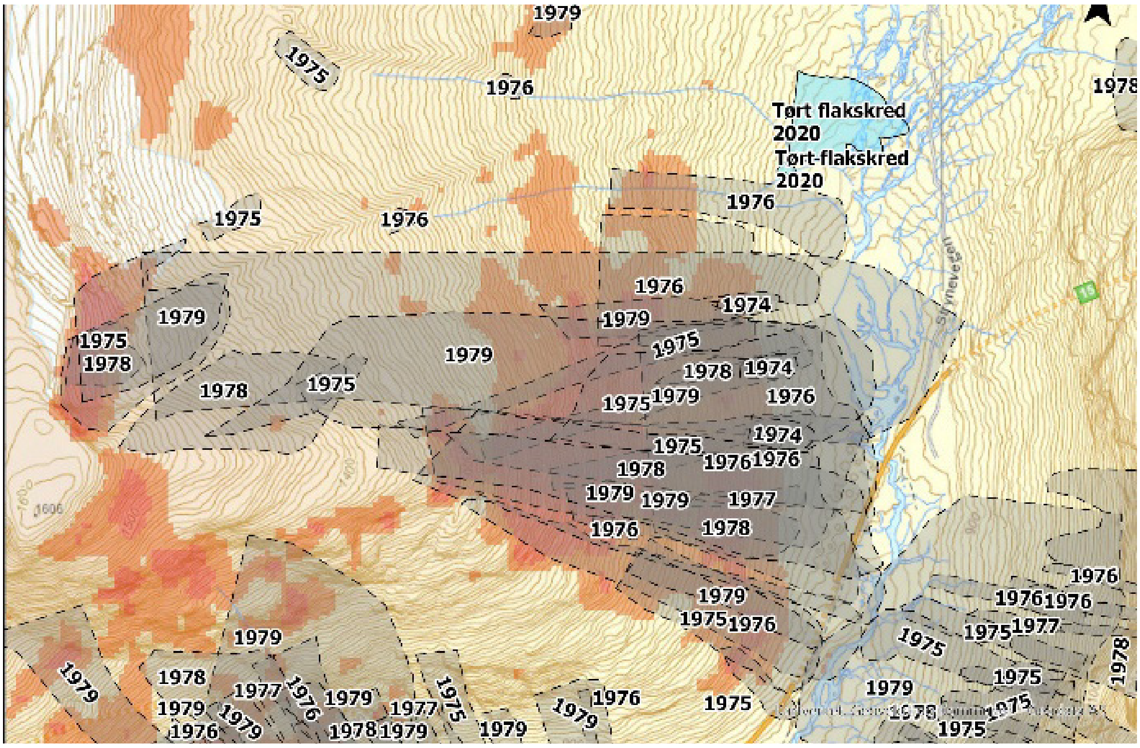

Figure 35: Winstral sheltering index for values above 0.6 (orange) and 0.7 (red) for wind direction from 270° at Sætreskarsfjellet. Observed avalanche paths are shown as grey polygons.

6.2 Wind-fields modelled with WindSim

WindSim is a Norwegian-developed state-of-the-art CFD modelling software built to optimize representation of wind. The software is also widely used for research on air pollution, icing on electricity lines etc., and was found to be the best alternative for testing a commercial CFD wind software package for snow transport. The software is prepared for rather coarse-resolution terrain models as input and high-altitude wind fields. For our purposes high-resolution terrain features are of interest as well as near-surface wind fields, and therefore available methods for input data generation and import could not be used. As there are no standard formats for input and output data of neither terrain, roughness nor climate data, but rather specific WindSim formats, an unforeseen amount of resources was used to develop tools to generate terrain data files from GIS, climate data input files and import routines of vector wind fields to GIS:

1. Tool for export of terrain and roughness data from ArcGISpro including stand-alone Python script to convert from ASCII format to .gws-format.
2. Script to generate input climatology file in tws-format (timeseries) for selected weather station – MATLAB.
3. ArcGIS Pro tool to import XY wind vector fields from WindSim and convert these into arrows and continuous wind speed raster.
4. Script to read and transfer validated climatologies to observed data – MATLAB.

WindSim has primarily been run based on the national 10 m DEM from the Norwegian Mapping Authority. However, the initial run must solve for unknown boundary conditions, and the area of the first run has to be large enough to both capture major topographical features and wind fields in the area, and the area of interest should be far from the edges in order to minimize boundary effects. In this study we have used two nestings for all test areas. In nesting 1 an area of around 10×10 km was typically chosen, with 20–25 vertical layers and a grid resolution of around 50 meters. In nesting 2 a smaller area of about 5x5 km was selected, with 20 vertical layers, and with a refined grid in the centre of the model area (see Gisnås, 2020for details).

Wind fields were generated for Grasdalen, Strynefjellet, Finse, Tyin and Stryn valley (for storm surge analysis). The results are validated with wind and snow distribution observations at Finse and Grasdalen. The results are presented in (Gisnås, 2020), while a short summary is presented below.

The model is validated against observed winds in the terrain by using the tool "transferred climatologies"; time series of observed wind observations from a point inside the model domain are transferred to time series of wind in another point within the model domain. Validation results from Finse show that WindSim is able to reproduce the main wind direction and speeds also in complex terrain with elevation differences of only 20–50 meters when the model is adjusted to fine resolution both in the horizontal and in the vertical plan near ground (Gisnås, 2020).

Vector fields and continuous velocity maps have been compared to release areas in Sæterskarsfjellet in Grasdalen. The model results from westerly wind direction (270°) modelled in Strynefjell_nest2_fonnbu2 shows that westerly winds tend to approach the lower part of the ridge from a south-westerly direction. As the valley side to the southwest is very steep, there is limited snow available for transport. In the upper part significant accumulation would be expected as the wind decelerates as it crosses the edge down from the plateau. In Figure 37 we find a low-speed area in the middle part of the ridge at Sætreskarsfjellet.

The results from the WindSim modelling at Strynefjellet show great potential for understanding snow deposition and distribution in potential release areas in connection to major wind directions in complex terrain. Detailed analyses are required to make use of the data, and for quick overviews a terrain index model will provide useful information at very little cost. However, to understand complex deposition patterns, and to track release probability in a specific potential release area to prevailing wind directions, complex physical models like WindSim model provide valuable input.

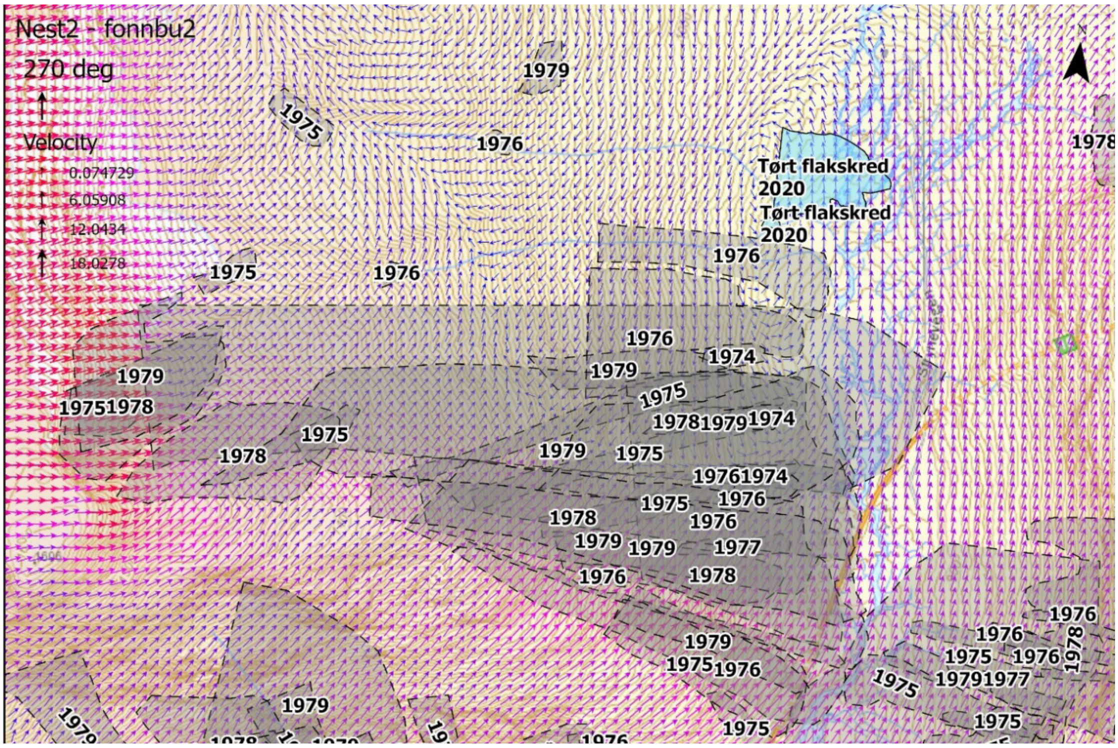

Figure 36: Vector field for wind from 270° at Sæterskarsfjellet exported from the Strynefjell_nest2_fonnbu2 model run. Observed avalanche paths are shown as grey polygons.

To further develop the method and suitability of CFD wind modelling for snow avalanche forecasting, a function to produce continuous rasters of acceleration and deceleration areas from vector fields should be developed. The effect of terrain resolution and vertical layers in the model setup should also be further explored. Information on snow accumulation in release areas in relation to specific storms would benefit validation of future studies.

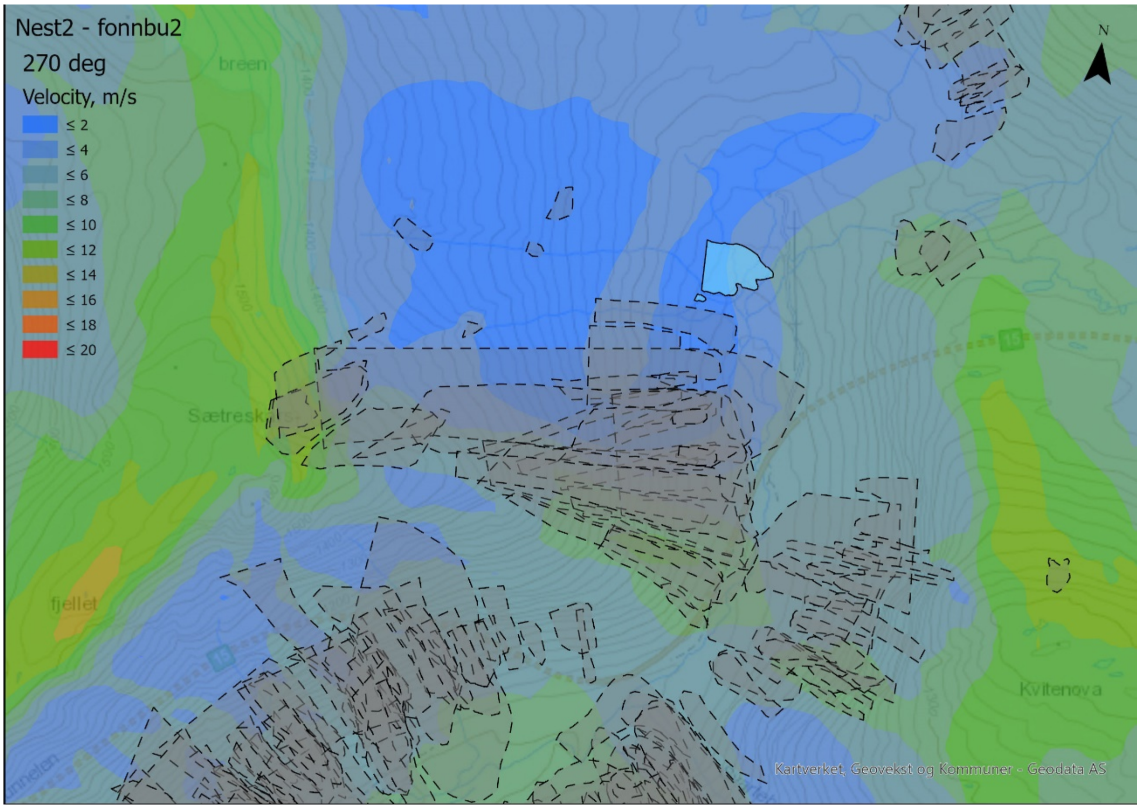

Figure 37: Velocity map for winds from 270° at Strynefjellet. Avalanche paths are shown as grey shaded polygons.

7 Work plan 2020–2022

The workplan for 2020–2022 is published on the NGI webpage (https://www.ngi.no/Prosjekter/AARN-Applied-Avalanche-Research-in-Norway). The focus areas for the next three years are:

WP1 – Avalanche formation

- Variable size of release areas and volumes
- Effects of wind and weather on the snowpack properties
- Simple probabilistic release models

WP2 – Avalanche motion / dynamics

- Mathematical avalanche model + Reasons for extreme runouts
- Avalanche experiments
- New instrumentation for avalanche dynamics research

WP3 – Avalanche interaction

- Alternative mitigation measures
- Vulnerability of structures and persons in buildings
- Residual risk

CPT – Cross Package Topics

- Climate and climate change
- Avalanche observations and monitoring
- Quantitative risk analysis
- Effect of forest
- Dissemination

8 References

Ancey, C. and Bain, V. (2015). Dynamics of glide avalanches and snow gliding. *Reviews of Geophysics* **53**, 745–784.

Bartelt, P., Bühler, Y., Christen, M., Deubelbeiss, Y., Salz, M., Schneider, M., and Schumacher, L. (2017). RAMMS User Manual v.1.7.0 Avalanche. WSL Institute for Snow and Avalanche Research SLF, Davos, Switzerland.

Bakkehøi, S., Domaas, U. and Lied, K. (1983). Calculation of snow avalanche runout distance. *Annals of Glaciology* **4**, 24–29.

Breien, H. (2019). Befaringsrapport Grandefonna, Geiranger [Survey report on the Grandefonna avalanche, Geiranger]. NGI Technical Note 20170131-14-TN [in Norwegian]. Norwegian Geotechnical Institute, Oslo, Norway.

Briukhanov, A. V., Grigorian, S. S., Miagkov, S. M., Plam, M. Y., Shurova, I. Y., Eglit, M. E. and Yakimov, Y. L. On some new approaches to the dynamics of snow avalanches. *In:* Ôura, H. (Ed.), Physics of Snow and Ice, Proc. Intl. Conf. Low Temperature Science, Sapporo, Japan, 1966. Institute of Low Temperature Science, Hokkaido University, Sapporo, Japan. Vol. I, Part 2, pp. 1223–1241.

Buser, O. and Frutiger, H. (1980). Observed maximum run-out distance of snow avalanches and the determination of the friction coefficients μ and ξ. *Journal of Glaciology* **26**(94), 121–130.

Chehata, D., Zenit, R. and Wassgren, C. R. (2003). Dense granular flow around an immersed cylinder. *Physics of Fluids* 15, 1522–1531.

Christen, M., Kowalski, J., and Bartelt, P. (2010). RAMMS: Numerical simulation of dense snow avalanches in three-dimensional terrain. *Cold Regions Science and Technology* **63**, 1–14.

Dorren, L. K. A. and Berger, F. (2005). Stem breakage of trees and energy dissipation during rockfall impacts. *Tree Physiology* **26**, 63–71.

Eckerstorfer, M., Malnes, E., Frauenfelder, R., Domaas, U. and Brattlien, K. (2014). Avalanche debris detection using satellite-borne radar and optical remote sensing. *In:* Proceedings of the International Snow Science Workshop 2014, Banff, Alberta, Canada, pp. 122–128. URL https://arc.lib.montana.edu/snow-science/objects/ISSW14_paper_O5.04.pdf.

Eglit, M. E. Raschet parametrov lavin v zone tormozhenija i ostanovki (Calculating avalanche parameters in the zone of slowdown and stopping). Materialy Glyatsologicheskikh Issledovaniye (Data of Glaciological Studies) **43**, 35–39.

Eglit, M. E. and Demidov, K. S. (2005). Mathematical modeling of snow entrainment in avalanche motion. *Cold Regions Science and Technology* **43**(1–2), 10–23. DOI 10.1016/j.coldregions.2005.03.005.

Elder, K. and Kattelmann, R. (1992). Observations of a slushflow on a low-angle slope in west Karakol Valley, Kirgizstan, Middle Asia. *In:* Proceedings of the International Snow Science Workshop 1992, Breckenridge, Colorado, USA, pp. 309–316.

Elder, K. and Kattelmann, R. (1993). A low-angle slushflow in the Kirgiz Range, Kirgizstan. *Permafrost and Periglacial Processes* **4**, 301–310.

Eybert-Bérard, A., Perroud, P., Brugnot, A. Mura, R., and Rey, L. (1978). Mesures dynamiques dans l'avalanche – résultats expérimentaux du Col du Lautaret (1972–1978). *In:* Proceedings of the Second International Meeting on Snow and Avalanches, 12–14 April 1978, Grenoble, France. Société Hydrotechnique de France and ANENA, Grenoble, France, pp. 203–224.

Feistl, T., Bebi, P., Bühler, Y., Christen, M., Teich, M. and Bartelt, P. (2012). Stopping behavior of snow avalanches in forests. *In:* Proceedings of the International Snow Science Workshop 2012, Anchorage, Alaska, pp. 420–426.

Frigo, B., B. Chiaia, I. Chiambretti, P. Bartelt, M. Maggioni and M. Freppaz (2018). The January 18th 2017 Rigopiano disaster in Italy – analysis of the avalanche dynamics. *In:* Proc. Intl. Snow Science Workshop 2018, Innsbruck, Austria, pp. 6–10. URL https://arc.lib.montana.edu/snow-science/objects/ISSW2018_O01.2.pdf.

Gauer, P. (2013). Comparison of avalanche front velocity measurements: supplementary energy considerations. *Cold Regions Science and Technology* **96**, 17–22.

Gauer, P. (2014). Comparison of avalanche front velocity measurements and implications for avalanche models. *Cold Regions Science and Technology* **97**, 132–150.

Gauer, P. (2018a). Considerations on scaling behavior in avalanche flow along cycloidal and parabolic tracks. *Cold Regions Science and Technology* **151**, 34–46.

Gauer, P., (2018b). Avalanche probability: Slab release and the effect of forest cover. *In:* Proceedings of the International Snow Science Workshop 2018, Innsbruck, Austria, pp. 76–83. URL https://arc.lib.montana.edu/snow-science/objects/ISSW2018_P01.13.pdf.

Gauer, P. (2018c) Estimates on the reach of the powder part of avalanches. *In:* Proceedings of the International Snow Science Workshop 2018, Innsbruck, Austria, pp. 815–819. URL https://arc.lib.montana.edu/snow-science/objects/ISSW2018_P08.23.pdf.

Gauer, P. and Issler, D. (2004). Possible erosion mechanisms in snow avalanches. *Annals of Glaciology* **38**, 384–392.

Gauer, P. and Kristensen, K. (2016). Four decades of observations from NGI's full-scale avalanche test site Ryggfonn—summary of experimental results. *Cold Regions Science and Technology* **125**, 162–176.

Gauer, P., Kronholm, K., Lied, K., Kristensen, K. and Bakkehøi, S. (2010). Can we learn more from the data underlying the statistical α-β model with respect to the dynamical behavior of avalanches? *Cold Regions Science and Technology* **62**, 42–54.

Gauer, P., Lied, K., and Kristensen, K. (2008). On avalanche measurements at the Norwegian full-scale test-site Ryggfonn. *Cold Regions Science and Technology* **51**, 138–155.

Gisnås, K. (2020). Wind simulations for use in local avalanche forecasting. NGI Technical Note 20170131-19-TN. Norwegian Geotechnical Institute, Oslo, Norway.

Grigorian, S. S. and Ostroumov, A. V. (2020). On a continuum model for avalanche flow and its simplified variants. *Geosciences* **10**, 35, DOI 10.3390/geosciences10010035.

Gude, M. and Scherer, D. (1998). Snowmelt and slushflows: hydrological and hazard implications. *Annals of Glaciology* **26**, 381–384.

Humstad. T., Søderblom, Ø., Ulivieri, G., Langeland, S., and Dahle, H. (2016). Infrasound Detection of Avalanches in Grasdalen and Indreeidsdalen, Norway. *In:* Proc. Intl. Snow Science Workshop 2016, Breckenridge. International Snow Science Workshop, pp. 621–627. URL https://arc.lib.montana.edu/snow-science/objects/ISSW16_P1.25.pdf.

Issler, D. (2019a). Field Survey of the 2017 Rigopiano Avalanche. NGI Technical Note 20170131-02-TN. Norwegian Geotechnical Institute, Oslo, Norway.

Issler, D. (2019b). Dynamical aspects of the 2017 Rigopiano avalanche. NGI Technical Note 20170131-08-TN. Norwegian Geotechnical Institute, Oslo, Norway.

Issler, D. (2020). Comments on "On a continuum model for avalanche flow and its simplified variants" by S. S. Grigorian and A. V. Ostroumov. *Geosciences* **10**, 96, DOI 10.3390/geosciences10030096.

Issler, D., Errera, A., Priano, S., Gubler, H., Teufen, B. and Krummenacher, B. (2008). Inferences on flow mechanisms from snow avalanche deposits. *Annals of Glaciology* **49**, 187–192. DOI 10.3189/-172756408787814915.

Issler, D., Gauer, P., Schaer, M. and Keller S. (1996). Staublawinenereignisse im Winter 1995: Seewis (GR), Adelboden (BE) und Col du Pillon (VD). SLF Internal Report 694. WSL Institute for Snow and Avalanche Research SLF, Davos, Switzerland, 1996. (In German)

Issler, D., Gauer, P., Schaer, M. and Keller S. (2020). Inferences on mixed snow avalanches from field observations. Geosciences 10(1), 2. DOI 10.3390/geosciences10010002. Supplementary Materials accessible at https://www.mdpi.com/2076-3263/10/1/2/s1.

Issler, D. and Jóhannesson, T. (2011). Dynamically consistent entrainment and deposition rates in depth-averaged gravity mass flow models. NGI Technical Note 20110112-01-TN, Norwegian Geotechnical Institute, Oslo, Norway. DOI 10.13140/RG.2.2.31327.71840.

Jóhannesson, T., Gauer, P., Issler, D., and Lied, K. (editors, 2009). The design of avalanche protection dams. Recent practical and theoretical developments. Climate Change and Natural Hazard Research Series 2, nr. EUR 23339. European Commission, Directorate-General for Research. ISBN 978-92-79-08885-8, ISSN 1018-5593.

Lackinger, B., 1989. Supporting forces and stability of snow-slab avalanches: a parameter study. *Annals of Glaciology* **13**, 140–145.

Lied, K. and Bakkehøi, S. (1980). Empirical calculations of snow-avalanche run-out distance based on topographic parameters. *Journal of Glaciology* **26**(94), 165–177.

Marchetti, E., Ripepe, M., Ulivieri, G., and Kogelnig, A. (2015). Infrasound array criteria for automatic detection and front velocity estimation of snow avalanches: towards a real-time early-warning system, *Natural Hazards and Earth System Sciences* **15**, 2545–2555, DOI: 10.5194/nhess-15-2545-2015.

McClung, D. M. (2000). Extreme avalanche runout in space and time. *Canadian Geotechnical Journal* **37**, 161–170.

McClung, D. M. and Gauer, P. (2018). Maximum frontal speeds, alpha angles and deposit volumes of flowing snow avalanches. *Cold Regions Science and Technology* **153**, 78–85.

McClung, D. M., Mears, A. I. and Schaerer, P. (1989). Extreme avalanche run-out: Data from four mountain ranges. *Annals of Glaciology* **13**, 180–184.

Mitterer, C., & Schweizer, J. (2013). Analysis of the snow-atmosphere energy balance during wet-snow instabilities and implications for avalanche prediction. The Cryosphere, 7(1), 205–216. https://doi.org/10.5194/tc-7-205-2013

Pérez-Guillén, C., K. Tsunematsu, K. Nishimura and D. Issler (2018). Avalanches on Mt. Fuji, Japan: seismic detection and tracking combined with numerical simulations. *In:* Proc. Intl. Snow Science Workshop 2018, Innsbruck, Austria, pp. 11–15. URL https://arc.lib.montana.edu/snow-science/objects/ISSW2018_O01.3.pdf.

Pérez-Guillén, C., Tsunematsu, K., Nishimura, K. and Issler, D. (2019). Seismic detection and tracking of avalanches and slush flows on Mt. Fuji, Japan. *Earth Surface Dynamics* **7**, 989–1007.

Rudolf-Miklau, F., Sauermoser, S., Mears, A. I. (Eds., 2014). The Technical Avalanche Protection Handbook. Ernst & Sohn, Berlin, Germany. ISBN 978-3-433-03034-9.

Sandersen, F. Snøskredulykke i Tamokdalen 2019-01-02 / Snow Avalanche Accident in the Tamok Valley, 2019-01-02. NGI Technical Note 20170131-13-TN rev. 2 [in Norwegian with English summary]. Norwegian Geotechnical Institute, Oslo, Norway.

Scherer, D., Gude, M. and Lange, G. (1996). Sulzströme – eine verkannte Gefahr. *Spektrum der Wissenschaft* **3**, 14–16.

Schläppy, R., Eckert, N., Jomelli, V., Stoffel, M., Grancher, D., Brunstein, D., Naaim, M. and Deschatres, M. (2014). Validation of extreme snow avalanches and related return periods derived from a statistical-dynamical model using tree-ring techniques. *Cold Regions Science and Technology* **99**, 12–26.

Serinaldi, F. (2014). Dismissing return periods! Stochastic Environmental Research and Risk Assessment. *Springer Nature* **29**, 1179–1189.

Sovilla, B., Burlando, P. and Bartelt, P. (2006). Field experiments and numerical modeling of mass entrainment in snow avalanches. *Journal of Geophysical Research* **111**, F03007.

Sovilla, B., Kern, M., and Schaer, M. (2010). Slow drag in wet snow avalanche flow. *Journal of Glaciology* **56**(198), 587–592.

Teich, M., Fischer, J.-T., Feistl, T., Bebi, P., Christen, M. and Grêt-Regamey, A. (2014). Computational snow avalanche simulation in forested terrain. *Natural Hazards and Earth System Sciences* **14**, 2233–2248.

Thibert, E., Faug, T., Bellot, H., and Baroudi, D. (2013). Avalanche impact pressure on a platelike obstacle. *In:* International Snow Science Workshop 2013, Grenoble and Chamonix–Mont-Blanc, pp. 663–670.

Ulivieri, G., Marchetti, E., Ripepe, M., Chiambretti, I., and Segor, V. (2012). Infrasonic monitoring of snow avalanches in the Alps. *In:* Proceedings of the International Snow Science Workshop 2012, Anchorage. International Snow Science Workshop, pp. 723–728. URL https://arc.lib.montana.edu/snow-science/objects/issw-2012-723-728.pdf.

Voellmy, A. (1964). On the destructive force of avalanches (translation by R. E. Tate). Translation 2, Alta Avalanche Study Center Wasatch National Forest.

NGI (2015). Results 2015 from SP 4 FoU Snøskred: Work Package 3 — Slushflows. Report from project 20140053, Norwegian Geotechnical Institute, Oslo, Norway.

Buisson, L. and Charlier, C. (1993). Avalanche modelling and integration of expert knowledge in the ELSA system. *Ann. Glaciol.* **18**, 123–128

Chernouss, P. A. and Yu. Fedorenko (2001). Application of statistical simulation for avalanche-risk evaluation. *Ann. Glaciol.* **32**, 182–186. DOI http://www.doi.org/10.3189/172756401781819274

Gauer, P., M. Kern, K. Kristensen, L. Lied, L. Rammer and H. Schreiber (2007). On pulsed Doppler radar measurements of avalanches and their implication to avalanche dynamics. *Cold Reg. Sci. Technol.* 50 (1–3), 55–71. DOI 10.1016/j.coldregions.2007.03.009

Issler, D., P. Gauer, K. Gladitsch Gisnås and U. Domaas (in prep.). Approaches to including climate and forest effects in avalanche hazard indication maps in Norway

Lackinger, B. (1989). Supporting forces and stability of snow-slab avalanches: a parameter study. *Ann. Glaciol*. **13**, 140–145

McClung, D. M. and P. Gauer (2018). Maximum frontal speeds, alpha angles and deposit volumes of flowing snow avalanches. *Cold Reg. Sci. Technol.* **153**, 78—85

Takeuchi, Y., K. Nishimura and A. Patra (2019). Observations and numerical simulations of the braking effect of forests on large-scale avalanches. *Ann. Glaciol.* **59**(77), 9 pp., DOI 10.1017/aog.2018.22

Kontroll- og referanseside/ Review and reference page

Dokumentinformasjon/*Document information*		
Dokumenttittel/*Document title* Annual Report 2019		**Dokumentnr./*Document no.*** 20170131-17-R
Dokumenttype/*Type of document* Rapport / Report	**Oppdragsgiver/*Client*** Norges vassdrags- og energidirektorat (NVE)	**Dato/*Date*** 2020-05-28
Rettigheter til dokumentet iht kontrakt/ *Proprietary rights to the document according to contract* Oppdragsgiver / Client		**Rev.nr.&dato/*Rev.no.&date*** 0 /
Distribusjon/*Distribution* BEGRENSET: Distribueres til oppdragsgiver og er tilgjengelig for NGIs ansatte / LIMITED: Distributed to client and available for NGI employees		
Emneord/*Keywords* Snow avalanches, full-scale experiments, field observations, dynamical and statistical models, slushflows, snowdrift		

Stedfesting/*Geographical information*	
Land, fylke/*Country*	**Havområde/*Offshore area***
Kommune/*Municipality*	**Feltnavn/*Field name***
Sted/*Location*	**Sted/*Location***
Kartblad/*Map*	**Felt, blokknr./*Field, Block No.***
UTM-koordinater/*UTM-coordinates* **Zone: East: North:**	**Koordinater/*Coordinates*** **Projection, datum: East: North:**

Dokumentkontroll/*Document control*
Kvalitetssikring i henhold til/*Quality assurance according to NS-EN ISO9001*

Rev/ *Rev.*	**Revisjonsgrunnlag/*Reason for revision***	**Egenkontroll av/ *Self review by:***	**Sidemanns-kontroll av/ *Colleague review by:***	**Uavhengig kontroll av/ *Independent review by:***	**Tverrfaglig kontroll av/ *Interdisciplinary review by:***
0	Original document	2020-05-26 Christian Jaedicke	2020-05-26 Graham Gilbert	2020-05-27 Dieter Issler	

Dokument godkjent for utsendelse/ *Document approved for release*	**Dato/*Date*** 28 May 2020	**Prosjektleder/*Project Manager*** Christian Jaedicke / Dieter Issler

2015-10-16, 043 n/e, rev.03

NGI (Norwegian Geotechnical Institute) is a leading international centre for research and consulting within the geosciences. NGI develops optimum solutions for society and offers expertise on the behaviour of soil, rock and snow and their interaction with the natural and built environment.

NGI works within the following sectors: Offshore energy – Building, Construction and Transportation – Natural Hazards – Environmental Engineering.

NGI is a private foundation with office and laboratories in Oslo, a branch office in Trondheim and daughter companies in Houston, Texas, USA and in Perth, Western Australia

www.ngi.no

NGI (Norges Geotekniske Institutt) er et internasjonalt ledende senter for forskning og rådgivning innen ingeniørrelaterte geofag. Vi tilbyr ekspertise om jord, berg og snø og deres påvirkning på miljøet, konstruksjoner og anlegg, og hvordan jord og berg kan benyttes som byggegrunn og byggemateriale.

Vi arbeider i følgende markeder: Offshore energi – Bygg, anlegg og samferdsel – Naturfare – Miljøteknologi.

NGI er en privat næringsdrivende stiftelse med kontor og laboratorier i Oslo, avdelingskontor i Trondheim og datterselskaper i Houston, Texas, USA og i Perth, Western Australia.

www.ngi.no

OSLO
TRONDHEIM
HOUSTON
PERTH

NORWEGIAN GEOTECHNICAL INSTITUTE
NGI.NO

Main office
PO Box 3930 Ullevaal St.
NO-0806 Oslo
Norway

Trondheim office
PO Box 5687 Torgarden
NO-7485 Trondheim
Norway

T (+47)22 02 30 00
F (+47)22 23 04 48
NGI@ngi.no

BIC NO. DNBANOKK
IBAN NO26 5096 0501 281
ORGANISATION NO.
958 254 318MVA

ISO 9001/14001
CERTIFIED BY BSI
FS 32989/EMS 612006